Journal of the Brazilian Society of Mechanical Sciences and Engineering (2020) 42:630
https://doi.org/10.1007/s40430-020-02605-x

TECHNICAL PAPER

Two-phase nanofluid flow simulation with different nanoparticle morphologies in a novel parabolic trough solar collector equipped with acentric absorber tube and insulator roof

Ali Akbar Abbasian Arani[1] · **Farhad Monfaredi**[1]

Received: 13 May 2020 / Accepted: 3 September 2020 / Published online: 19 November 2020

Abstract

The main objective of the present work is to investigate the morphology effects of Syltherm 800 oil-based γ-AlOOH nanofluid on performance evaluation criterion (PEC) and energy efficiency of a novel parabolic trough solar collector (PTSC) numerically using finite volume method. The other goal is to compare the obtained results of nanofluid simulation in PTSC using single-phase mixture model (SPM) with two-phase mixture model (TPM). In addition, influences of using acentric absorber tube are determined. Consequently, in this step the optimum configuration is introduced and then different nanofluids characteristics such as volume fractions, nanoparticles diameters and shapes on the optimum configuration are investigated. Based on the obtained results, for all studied cases, obtained PEC and energy efficiencies employing the TPM in nanofluid simulation are more than that SPM simulation. Using the novel PTSC leads to the higher average Nusselt number, energy efficiency, PEC and outlet temperature at all Reynolds numbers. For all cases, the PEC and energy efficiency increase by reduction of nanoparticle volume fraction and diameter. As the Reynolds number increases, the energy efficiency of PTSC increases for all studied cases till Reynolds number equal to 5000 and then always reduces. Therefore, the optimum Reynolds number is 5000. The optimum morphology is related to the nanoparticles shape of blade which is followed by the brick, cylinders and platelet, respectively.

Keywords Parabolic trough solar collector (PTSC) · Nanofluid · Morphology · Nanoparticle shape · Two-phase mixture model (TPM) · Single-phase mixture model (SPM)

1 Introduction

Developing energy solicitations have encouraged the expansion of novel archetypes for the utilization of renewable energies [1]. Nowadays, parabolic trough solar collectors (PTSCs) that are used in solar power plants and thermic applications are investigated by several authors for their increased performance evolution criteria (PEC) [2–13]. For surface-based receivers, the spectral elective absorption cover and vacuum insulating have been commonly needed to achieve more temperatures for industrial and commercial employment. The elective cover on the absorbing plate might enhance the thermal performance by 30% as an outcome of reducing the emissivity coefficient to 0.10. The vacuum reduced the convectional heat wastes from the absorbing plate and barricaded the demotion of the covering at high temperatures. Howsoever, the elective cover tolerated the hazard of oxidation and demotion in state of long-term inflicted thermal stresses or vacuum missing. However, the permanence of covering and the vacuum insulating technology is enhanced in recent times; a giant price would be involved too. Volumetric-based receivers, notwithstanding being non-elective, might snare further thermal energy, improve the heat transfer process and consequently lead to a more thermal efficiency.

Bellos et al. [3] present a study on the exergetic and energetic improvement of parabolic trough solar collector equipped with absorber tube having internal fins filling with

Technical Editor: Ahmad Arabkoohsar.

This article has been selected for a Topical Issue of this journal on Nanoparticles and Passive-Enhancement Methods in Energy.

✉ Ali Akbar Abbasian Arani
abbasian@kashanu.ac.ir

1 Department of Mechanical Engineering, University of Kashan, Ravand Blv., Kashan, Iran

carbon dioxide at high temperature. Their results showed that higher fins length improved the thermal performance. They reached 46% exergetic efficiency with 400 °C as inlet temperature. Their analysis is done with SolidWorks Flow simulation. In another investigation, Bellos and Tzivanidis [4] presented an investigation on the effect of different technique as internal fins, ring inserts, dimpled absorbers and metallic foams on improvement of thermal efficiency of parabolic trough solar collector. They reported that referred technique can improve the thermal performance up to 2% with 600 K as inlet temperature. In addition, in referred case the thermal loss is 22% lower than respective reference case. Li et al. [6] focused on the conduction and radiation heat loss from the parabolic trough solar and effect on the thermal efficiency accompanied with operating cost. They analyzed various factors that influenced the heat losses such as glass envelope temperature, gas species, annulus pressure, heat transfer fluid temperature, size and aspect ratio of annulus. In addition, they present a theoretical basis in order to enhance receiver. Aldulaimi [7] proposed a new technique through an experimental investigation in order to improve the absorber tube of a parabolic trough collector efficiency employing a twisted tube. Proposed design was related to the reverse flow and overlapped. Presented results showed a significant increase for heat transfer enhancement. They reported that employed technique was accompanied by an increase in the pressure drop. For employed model, a factor that contains the pressure drop and Nusselt number named as evaluation criterion was defined and used. Khan et al. [11] performed a numerical investigation on the three different absorber tube geometries employed in parabolic trough solar collector (inserted twisted tape, longitudinal fins and smooth absorber tube) in the presence of Al_2O_3/water nanofluid as working fluid. Their outcome showed that absorber tube thermal efficiency accompanied with twisted tape insert filling with nanofluid and that for absorber tube accompanied with internal fins filling with nanofluid are about 72%.

It is three decades that the word of *nanofluids* are presented to the technical society. In detail in the nanofluids, higher thermal conductivity of solid particles relative to fluid enhances effectively the thermal conductivity of suspensions [14]. Higher thermal conductivity of suspension (nanofluids) must be related to the various parameters such as material type, temperature, volume fraction, shape and size. Several investigations have been done to assign the influence of refereed factors on the nanofluid thermal conductivity augmentation. Abbasian Arani et al. [15] conducted a numerical investigation for the particle shape effect (oblate spheroid, spherical, blade, platelet, prolate spheroid, and brick, and cylindrical) on the heat transfer and fluid flow of γ-AlOOH/ethylene glycol and water (50:50) nanofluid for the forced convection inside the minichannel having sinusoidal wavy wall. They provided the optimal shaped nanoparticle by evaluating the PEC and choosing the shape with the highest PEC. Based on their results, it is recognized that the best cases are corresponded to the *spherical*-shaped nanoparticles having nanoparticles volume fraction equal to 4% with diameter of 20 nm and Reynolds number of 15,000. Vanaki et al. [16] conducted a numerical study to investigate the influence of various nanofluid on the fluid flow and heat transfer inside the wavy wall channels. The objective of their investigation is to examine the influence of SiO_2/water nanofluid, its volume fraction and shape of nanoparticle (blade, cylindrical, platelet, spherical and brick), on the fluid flow and heat transfer. They showed that the SiO_2/EG nanofluids having the *platelet* particle present the maximum enhancement in heat transfer compared to the other studied nanofluids. Mahian et al. [17] presented an investigation on the influence of shape of nanoparticle by employing the laws of thermodynamics analysis (first and second laws) inside a minichannel of a solar collector with γ-AlOOH/water nanofluids as working fluid. Various nanoparticles shapes considering platelets, cylinders, bricks and blades are chosen for referred study. Based on analysis of entropy generation, inside the copper tubes, the minimum entropy generation is obtained employing *brick*-shaped nanoparticles, while for the steel tubes, the optimum entropy generation (minimum) is accomplished by employing the *blade*-shaped nanoparticles. Ooi and Popov [18] conducted a numerical study on the effects of particle shape in natural convection of Cu/water nanofluid. The influence of the spheroidal (NPs) and spherical particles (NPs) on the nanofluid natural convection is investigated. Their results provided that the highest enhancement in the overall heat transfer corresponded to the *oblate spheroid* nanoparticle having aspect ratio equal to 10. Elias et al. [19] conducted an investigation on the shape effect of γ-AlOOH nanoparticle for thermodynamic performance and heat transfer inside a shell-and-tube heat exchanger. The aim of referred study is to investigate the nanoparticle morphology effect (including brick, cylindrical, blade, spherical and platelet) on the heat exchanger thermal performance with nanofluid as working fluid. Their results provided that, between the all studied cases, *cylindrical*-shaped particles presented the highest rate of heat transfer. In another investigation, Elias et al. [20] studied the γ-AlOOH particle shapes effects on the shell-and-tube heat exchanger with various baffle angles with nanofluid. The objective of their investigation was to present the influence of various alumina nanoparticle shapes on the entropy generation, heat transfer and heat transfer coefficient. Based on their results, an increase of 28.23% in heat transfer coefficient for 20° baffle angle higher than that of 50° baffle angles is observed for *cylindrical* shape nanoparticles. The influence of various molybdenum disulfide (MoS_2)/water nanofluid morphologies for magneto-hydrodynamic slip flow in the presence of porous medium is investigated by Khan [21].

His results showed that nanoparticles having the *platelet* and *blade* shapes enhanced the heat transfer higher than that the brick and cylinder shapes. Hajabdollahi and Hajabdollahi [22] conducted an investigation on the influence of various aluminum dioxide nanoparticles shapes (blade, platelet, brick and cylindrical shapes) on the thermoeconomic enhancement of a shell-and-tube heat exchanger. Obtained results displayed that the maximum enhancement in thermoeconomic is accomplished employing the nanoparticles with *bricks* shape.

Table 1 reports a review of almost all investigations which study the morphology effects on thermal–hydraulic performances of nanofluid flow in various heat exchangers and solar receivers. In this table, all important parameters of these studies such as study type, geometry, nanofluids properties (base fluid and nanoparticles), types of investigated morphologies, most important results and finally the optimum nanoparticle shape in operating conditions are presented. As it is seen in Table 1, the effects of different nanoparticles shapes on thermal or hydraulic parameters of various heat exchangers are investigated during several numerical and experimental studies [14–33]. It is realized that different morphologies are adopted for different nanoparticles, nanofluids, geometries and boundary conditions. Therefore, it is found that for different conditions unlike morphologies effect are expected. It should be noted that, among all investigations in Table 1, just two papers [29, 31] deal with the study of morphology effects using *two-phase mixture model* (TPM), while in the other papers different nanoparticles shapes effect are studied with single-phase mixture model (SPM). Hence, the main objective of the present work is to study the morphology effects of Syltherm 800 oil-based γ-AlOOH nanofluid flow on the thermal–hydraulic performances and energy efficiency of a novel parabolic trough solar collector employing the TPM. Nanofluid-based PTSC, with suspended nanoparticles in base fluids, presented as a scientifically application. With an accurate design, the nanofluid average temperature might be more than that the absorbing plate, because the solar irradiance is absorbed by nanofluid directly [1].

Kaloudis et al. [34] investigated numerically a PTSC filled with Syltherm 800 liquid oil-based nanofluid as working fluid using TPM. Three modes of heat transfer (convection, conduction and radiation) were determined to simulate the PTSC. Their validation presented remarkable coincidence between the numerical results and experimental data. In order to simulate the nanofluid, both SPM and TPM were chosen and validated with empirical data and numerical results. Benabderrahmane et al. [35] investigated numerically the alumina/dowtherm-A nanofluid forced convection through a 3D PTSC equipped with vortex generators for heat transfer enhancement using SPM and TPM in turbulent flow regime. The numerical results are validated by comparing with the empirical data available in the literature, while very good agreement is obtained. The obtained results showed that TPM provided a greater coefficient of convective heat transfer than that SPM, while the calculated Darcy friction factor by SPM and TPM is basically the same.

The literature review shows that although the influence of different morphology effects using SPM on the thermal and hydraulic performances of different heat exchangers has been investigated, to the best of author's literature review it is not any investigation which presents different nanoparticle shapes effects using TPM on the thermal–hydraulic parameters and energy efficiency of a novel PTSC equipped with insulator roof with different arc-angles and acentric absorber tube filled with nanofluid. One of the objectives of this study is to investigate the effect of using the insulator roof with different arc-angles and acentric absorber tube in a PTSC which is filled with nanofluid numerically employing the finite volume method. The other goal of present study is to compare the obtained numerical results of simulating nanofluid in PTSC using SPM and TPM. The main objective of current investigation is to study the morphology effects of Syltherm 800 oil-based γ-AlOOH nanofluid flow on thermal–hydraulic performances and energy efficiency of a novel PTSC. In the first step, influences of using SPM or TPM in simulation of nanofluid in absorber tube are investigated, and then influences of using insulator roof and its different parameters have been studied. In the next step, influences of using acentric absorber tube are determined. Consequently in this step, the optimum configuration is introduced and in the last step different nanofluid parameters (different volume fraction, various nanoparticles diameters and morphologies) effect on the optimum configuration is investigated using TPM. To fulfill these demands, results of interests such as pressure drop, Nusselt number, outlet temperature, friction factors, energy efficiency and performance evaluation criteria are presented to demonstrate the influence of different conditions on studied parameters.

2 Methodology

2.1 Physical model and materials

Figure 8 illustrates the schematic diagram of a *conventional PTSC* (C.PTSC) and a *novel PTSC* (N.PTSC) equipped with roof-insulator and acentric absorber tube. For both PTSCs the annulus which is located among the absorber tube and glass cover is filled with ambient air lower than 0.83 atm. One of the main ideas in the present work is to fill the outward facing of the air-filled annulus with a heat-resistant insulating material, e.g., glass wool, and therefore find the optimum arc-angle of this roof-insulator. Also, it is expected that in the case of using acentric absorber tube, the heat

Table 1 A review of almost all investigations which study the morphology effects on the thermal and hydraulic performances of nanofluid flow in the different heat exchangers and solar receivers

Investigation	Type of study	Geometry	Nanofluid		Studied nanoparticle shapes	Outputs	Optimum shape
			Base fluid	Nanoparticles			
Avella et al. [23]	Exp.	Calorimeter	Water	$CaCO_3$	Spherical and elongated (see Fig. 1)	Outlet temperature	Elongated
Timofeeva et al. [14]	Exp.	Calorimeter	Water and ethylene glycol mixture (50:50)	γ-AlOOH	Platelet, spherical, cylindrical, blade, and brick (see Fig. 2)	Thermal conductivity enhancement	Blades
Elias et al. [19]	Num.	Shell-and-tube heat exchanger	Water and ethylene glycol mixture (50:50)	γ-AlOOH	Platelet, spherical, cylindrical, blade, and brick (see Fig. 2)	Heat transfer rate and entropy generation	Cylindrical
Fang et al. [24]	Exp.	Calorimeter	Ethylene glycol	Ag	Nanosphere, nanowire and nanoflakes (see Fig. 3)	Thermal conductivity enhancement	Nanowire
Ferrouillat et al. [25]	Exp.	Channel	Water	SiO_2 and ZnO	SiO_2 (spherical and bananas) (see Fig. 4) ZnO (polygonal ((Nyacol)) and Evonik) (see Fig. 5)	Nusselt number	SiO_2 (spherical), ZnO (Nyacol)
Ooi and Popov [18]	Ana.	Cavity	Water	Cu	Spherical, spheroidal (oblate and prolate) (see Fig. 6)	Nusselt number	Oblate spheroid
Elias et al. [20]	Num.	Baffled shell-and-tube heat exchanger	Water and ethylene glycol mixture (50:50)	γ-AlOOH	Platelet, spherical, cylindrical, blade, and brick (see Fig. 2)	Heat transfer and entropy generation	Cylindrical
Mahian et al. [17]	Ana.	Minichannel-based solar collector	Water and ethylene glycol mixture (50:50)	γ-AlOOH	Platelet, spherical, cylindrical, blade, and brick (see Fig. 2)	Nusselt number and entropy generation	Bricks
Vanaki et al. [16]	Num.	Sinusoidal wavy minichannel	Water	SiO_2	Platelet, spherical, cylindrical, blade, and brick (see Fig. 2)	Performance evaluation criteria index (PEC)	Platelets
Ellahi et al. [26]	Num.	Wedge	HFE-7100 Engineered Fluid	Nimonic 80a metal nanoparticles	Spherical, needle and disk	Bejan number and entropy generation	Needle
Karimi-Nazarabad et al. [27]	Exp.	Calorimeter	Ethylene glycol	WO_3	Spherical, polygonal and blade	Thermal conductivity enhancement	Polygonal
Abbasian Arani et al. [15]	Num.	Novel sinusoidal wavy minichannel	Water and ethylene glycol mixture (50:50)	γ-AlOOH	Spherical, platelet, blades, cylindrical, brick and spheroidal (oblate and prolate) (see Figs. 2, 6)	Performance evaluation criteria index (PEC)	Spherical
Hajabdollahi and Hajabdollahi [22]	Ana.	Shell-and-tube heat exchanger	Water	Al_2O_3	Platelet, spherical, cylindrical, blade, and brick (see Fig. 2)	Total annual cost (TAC)	Bricks

Table 1 (continued)

Investigation	Type of study	Geometry	Nanofluid		Studied nanoparticle shapes	Outputs	Optimum shape
			Base fluid	Nanoparticles			
Khan [21]	Ana./Num.	Porous medium channel	Water	MoS_2	Platelet, spherical, cylindrical, blade, and brick (see Fig. 2)	Heat transfer rate	Blade and platelet
Sheikholeslami and Bhatti [28]	Num.	Channel with porous media	Water	CuO	Spherical, platelet, cylindrical and brick (see Fig. 2)	Nusselt number	Platelets
Monfared et al. [29]	Num.	Double-pipe heat exchanger	Water and ethylene glycol mixture (50:50)	γ-AlOOH	Spherical, platelet, cylindrical and brick (see Fig. 2)	Entropy generation and Bejan number	Spherical
Al-Rashed et al. [30]	Num.	Minichannel heat exchanger	Water and ethylene glycol mixture (50:50)	γ-AlOOH	Spherical, platelet, cylindrical and brick (see Fig. 2)	Entropy generation and Bejan number	Spherical
Alsarraf et al. [31]	Num.	Double-pipe minichannel	Water and ethylene glycol mixture (50:50)	γ-AlOOH	Spherical, platelet, cylindrical and brick (see Fig. 2)	Heat transfer rate	Spherical
Sadripour and Chamkha [32]	Num.	Heat sink solar collector	Water	Cu, Ag, Al_2O_3 γ-AlOOH, MoS_2 SiO_2	Spherical, nanowire, platelet, blade, cylindrical, brick and spheroidal (oblate and prolate) (Figs. 2, 6, 7)	Nusselt number, outlet temperature and entropy generation	Spherical
Shahsavar et al. [33]	Num.	Double-pipe minichannel	Water and ethylene glycol mixture (50:50)	γ-AlOOH	Spherical, platelet, cylindrical and brick (see Fig. 2)	Heat transfer rate and pressure drop	Platelets

Table 2 Detailed geometrical parameters of the studied PTSC

Geometrical parameters	Values
Length of PTSC, L_{PTSC}	4.06 m
Outer diameter of absorber tube, d_a	0.07 m
Thickness of absorber tube, δ_a	0.003 m
Outer diameter of glass cover, d_g	0.12 m
Aperture of PTSC, $\mathcal{A}_{PTSC}$	0.525 m
Rim angle, ς_{Rim}	15°
Non-parallelism angle, ς_{NP}	16′

loss will reduce because of more insulator volume above the absorber tube. As it is seen in Fig. 8b, the novel receiver is included of a glass cover, an absorber tube, air-filled annulus and a roof-thermal-insulator (glass wool) which is filled in the other annulus part. As it is shown in Fig. 8, the solar energy is collected with the reflector and then is passed across the glass tube and to be absorbed by the absorber tube.

Table 2 reports the detailed geometrical parameters of the studied PTSC. Also as it is seen in Fig. 8b, two various geometrical parameters will be optimized in the present study based on the maximum energy efficiency which are insulator arc-angle (Ψ) and acentric value (Λ). Seven different arc-angle values ($\Psi = 30°, 50°, 70°, 90°, 110°, 120°$ and $150°$) and five various acentric values ($\Lambda = 0, 5, 10, 15$ and 20 mm) are investigated in this work.

Also, six different mass flow rates are studied which are in connection with corresponding Reynolds numbers as follows: 0.107 kg/s (Re = 2985.9), 0.161 kg/s (Re = 4001.7), 0.214 kg/s (Re = 5020.9), 0.321 kg/s (Re = 7063.2), 0.428 kg/s (Re = 9107.2) and 0.535 kg/s (Re = 11,151.6). It is clear that all studied mass flow rates are in turbulent flow regime.

For all studied cases, the direct normal irradiance is $I_b = 1000$ W/m^2, wind velocity is $V_w = 2.5$ m/s, ambient (environment) temperature is $T_{env} = 297.5$ K, and inlet nanofluid temperature is $T_{in} = 300$ K. The glass cover is prepared with Pyrex glass antireflective coated, and its properties are found in Table 3. The absorber tube is prepared from stainless steel and has a cermet selective surface, and its thermophysical properties are also listed in Table 3. Also the annulus is filled with air and the insulator material is glass wool and Table 3 reports their properties [15, 36, 37]. The heat transfer fluid is Syltherm 800 oil, and its properties could be approximated by following polynomial [38, 39]:

$$f(T) = a_0 + a_1T + a_2T^2 + a_3T^3 + a_4T^4, \tag{1}$$

where T is the fluid temperature (K). The function $f(T)$ in this equation can be $\rho(T)$, $c_p(T)$, $k(T)$ or $\mu(T)$. Also different coefficients in this equation can be found for each parameter in Table 4. This equation is valid for the temperature range between 300 and 650 K.

In the present study, boehmite alumina (γ-AlOOH) nanoparticles are be used and their properties are found in Table 3. The nanofluid properties (Syltherm 800 oil/γ-AlOOH) can be evaluated from Eqs. (2)–(10). Once again it should be referred that the emphasis of current study is on the modeling approach and on the calculating of performance employing the TPM relative to the SPM in studied problem.

Table 3 Properties of the Pyrex glass and stainless steel [15, 36, 37]

Property	Symbol (unit)	Pyrex glass	Stainless steal	γ-AlOOH	Air	Glass wool
Transmittance	τ (–)	0.95	–	–	–	–
Refractive index	ϱ (–)	1.474	–	–	–	–
Absorptance	α (–)	–	0.96	–	–	–
Emittance	ε (–)	–	0.14	–	–	–
Density	ρ (kg/m^3)	2.23×10^{-3}	7920	3050	1.125	18
Specific heat	c_p (J/kg K)	750	444	618.3	1006.43	670
Thermal conductivity	k (W/m K)	1.14	16	30	0.0242	0.04
Dynamic viscosity	μ (Pa s)	–	–	–	1.789×10^{-5}	–

Table 4 Correlations for the Syltherm 800 properties [38, 39]

Property	ρ (kg/m^3)	c_p (J/kg K)	k (W/m K)	μ (Pa s)
a_0	1.26903060×10^3	1.10787577×10^3	0.19011994	8.486612×10^{-2}
a_1	-1.52080898	1.70742274	$-1.88022387 \times 10^{-4}$	-5.541277×10^{-4}
a_2	$1.79056397 \times 10^{-3}$	0	0	1.388285×10^{-6}
a_3	$-1.67087252 \times 10^{-6}$	0	0	-1.566003×10^{-9}
a_4	0	0	0	6.672331×10^{-13}

For determining the nanofluid thermophysical properties of spherical nanoparticle, mixture theory is employed. The nanofluid density ρ_{nf} and nanofluid heat capacity $c_{\mathrm{P,nf}}$ at each section temperature (T_{m}) are evaluated with the following equations [40]:

Density:

$$\rho_{\mathrm{nf}} = (1-\phi)\rho_{\mathrm{bf}} + \phi\rho_{\mathrm{np}}. \quad (2)$$

Heat capacity:

$$c_{\mathrm{P,nf}} = \frac{(1-\phi)\left(\rho c_{\mathrm{P}}\right)_{\mathrm{bf}} + \phi\left(\rho c_{\mathrm{P}}\right)_{\mathrm{np}}}{\rho_{\mathrm{nf}}}. \quad (3)$$

Nanofluid thermal conductivity:

By introducing the particles Brownian motion, the nanofluid thermal conductivity can be estimated with Corcione's [40] correlation:

$$\frac{k_{\mathrm{eff}}}{k_{\mathrm{bf}}} = 1 + 4.4\mathrm{Re}_{\mathrm{np}}^{0.4}\mathrm{Pr}_{\mathrm{bf}}^{0.66}\phi^{0.66}\left(\frac{T}{T_{\mathrm{fr}}}\right)^{10}\left(\frac{k_{\mathrm{np}}}{k_{\mathrm{bf}}}\right)^{0.03}, \quad (4)$$

where $\mathrm{Re}_{\mathrm{np}}$ refers to the Reynolds number of particles, Pr refers to the base fluid Prandtl number, T refers to the temperature of nanofluid, T_{fr} refers to the base fluid freezing point, k_{np} refers to the thermal conductivity of nanoparticle, and ϕ refers to the nanoparticles volume fraction. The Reynolds number of nanoparticle is calculated as [40]:

$$\mathrm{Re}_{\mathrm{np}} = \frac{\rho_{\mathrm{bf}} u_{\mathrm{B}} d_{\mathrm{np}}}{\mu_{\mathrm{bf}}}, \quad (5)$$

where μ_{bf} and ρ_{bf} refer to the base fluid viscosity and density, respectively, and u_{B} and d_{np} refer to the Brownian velocity and nanoparticle diameter, respectively. With non-appearance of agglomeration, the Brownian velocity of nanoparticle, u_{B}, is estimated with the ratio of d_{np} and τ_D that is the time required to pass such distance [41]:

$$\tau_D = \frac{d_{\mathrm{np}}^2}{6D} = \frac{\pi\mu_{\mathrm{bf}} d_{\mathrm{np}}^3}{2k_{\mathrm{b}}T}, \quad (6)$$

where D and k_{b} refer to the Einstein diffusion and Boltzmann's constant, respectively [40]:

$$u_{\mathrm{B}} = \frac{2k_{\mathrm{b}}T}{\pi\mu_f d_{\mathrm{np}}^2}. \quad (7)$$

By substituting Eq. (7) in Eq. (5), it is obtained that [40]:

$$\mathrm{Re}_{\mathrm{np}} = \frac{2\rho_{\mathrm{bf}} k_{\mathrm{b}} T}{\pi\mu_{\mathrm{bf}}^2 d_{\mathrm{np}}}. \quad (8)$$

It is worth to refer that the physical properties in precedent equation are determined at the nanofluid temperature T.

Dynamic viscosity [40]:

$$\frac{\mu_{\mathrm{eff}}}{\mu_{\mathrm{bf}}} = \frac{1}{1 - 34.87\left(\frac{d_{\mathrm{np}}}{d_{\mathrm{bf}}}\right)^{-0.3}\phi^{1.03}}, \quad (9)$$

where d_{bf} is the base fluid equivalent diameter of molecule, given by [40]:

$$d_{\mathrm{bf}} = 0.1\left(\frac{6M}{N\pi\rho_{f0}}\right)^{1/3}, \quad (10)$$

where M and N refer to the base fluid molecular weight and Avogadro number, respectively, and ρ_{f0} refers to the base fluid density calculated at temperature $T_0 = 293$ K.

Also, four different non-spherical nanoparticle shapes such as blade, platelet, brick and cylindrical are compared in current study. Figure 2 presents a schematic of different shapes of the particles accompanied with their sizes [14].

The ρ_{nf} and $c_{\mathrm{p,nf}}$ of the nanofluids having various shapes can be determined with Eqs. (2) and (3), respectively. To present the influence of blades, platelets, bricks and cylindrical nanoparticle shapes on the nanofluid thermophysical properties, the following relations are employed [14]:

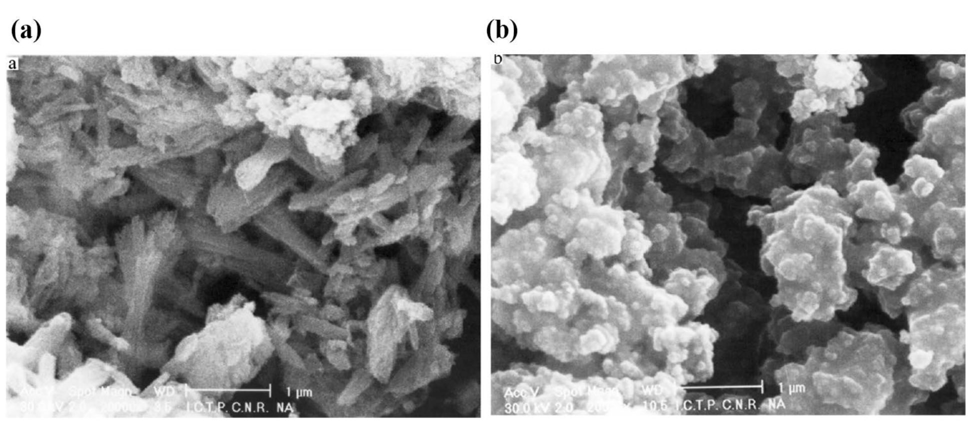

Fig. 1 Electron micrographs of the different shapes of $CaCO_3$ nanoparticles: **a** elongated, **b** spherical [23]

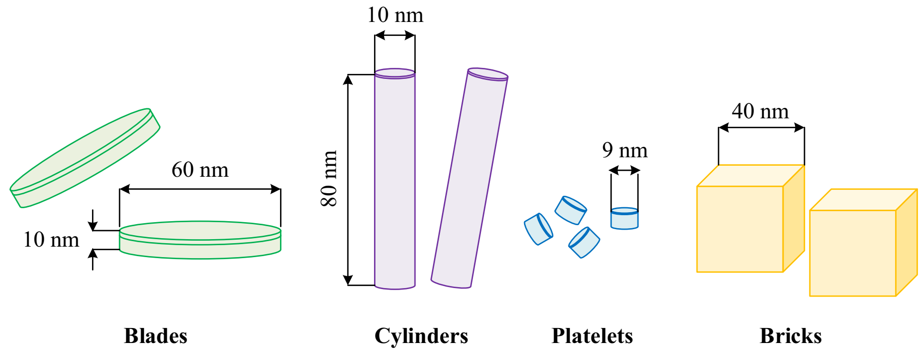

Fig. 2 Different shapes of nanoparticles used in the studies [14–17, 19, 21, 22, 26, 28–33]

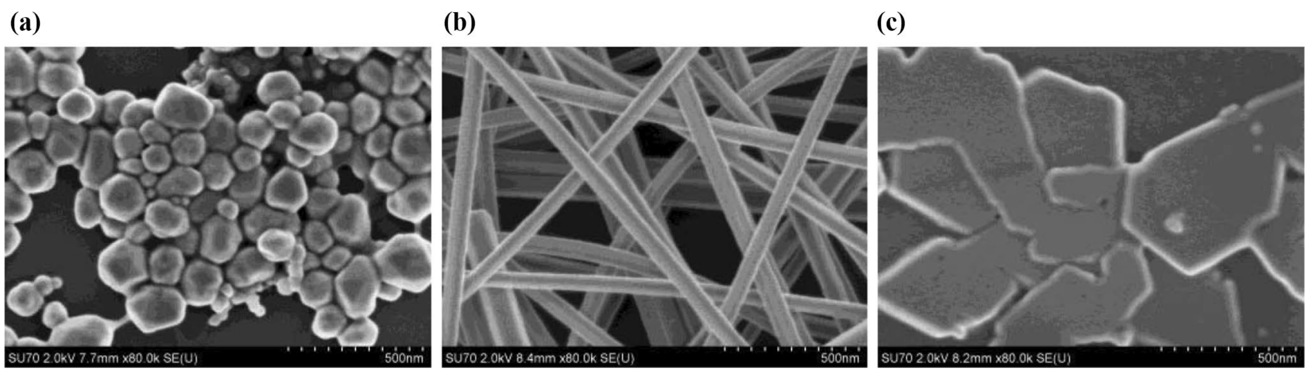

Fig. 3 Different shapes of the **a** Ag nanosphere, **b** Ag nanowire and **c** Ag nanoflakes [24, 32]

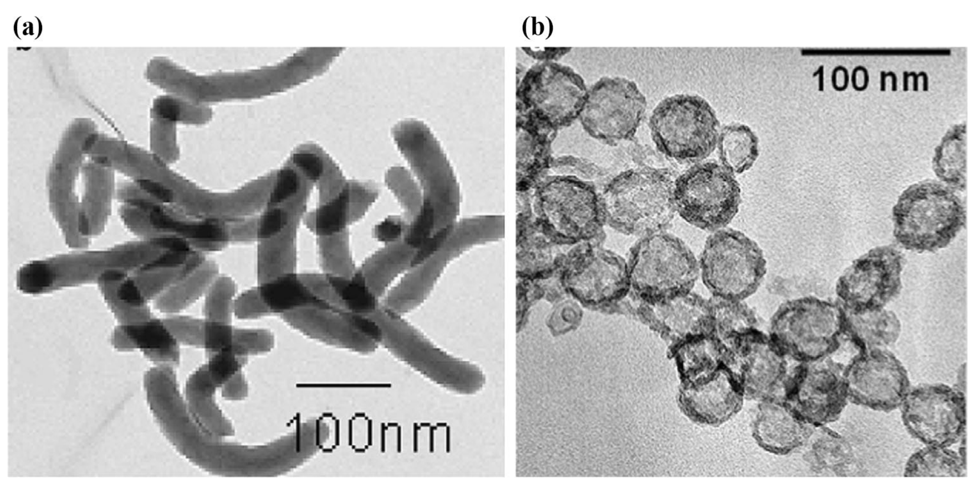

Fig. 4 TEM photograph of the SiO_2 nanoparticles: **a** nanoparticles with a shape factor (bananas); and **b** spherical nanoparticles [25]

$$\frac{k_{\text{eff}}}{k_f} = 1 + \left(C_k^{\text{shape}} + C_k^{\text{surface}}\right)\phi = 1 + C_k\phi. \tag{11}$$

The various nanoparticle shape effective thermal conductivities are determined employing the data available in Table 5.

$$\frac{\mu_{\text{eff}}}{\mu_f} = 1 + A_1\phi + A_2\phi^2, \tag{12}$$

where A_1 and A_2 are constant presented in Table 6.

2.2 Energy balance

As it was noted previously, Syltherm 800 oil/γ-AlOOH nanofluid is employed as working fluid and is flowed through

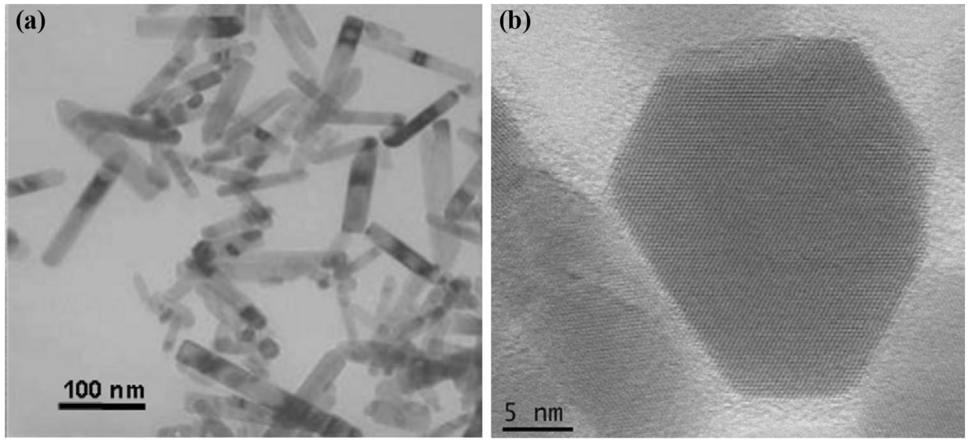

Fig. 5 **a** TEM of the ZnO particles with a shape factor (Evonik) and **b** HRSTEM image of the ZnO polygonal particles (Nyacol) [25]

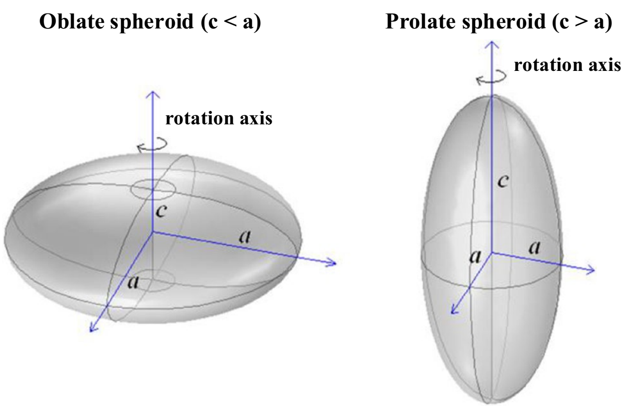

Fig. 6 The prolate and oblate spheroids [18, 32]

the absorber tube in simulated PTSC. Different heat transfer mechanisms are illustrated in Fig. 9 inside the PTSC. As it is presented in this figure, reflected solar irradiance is concentrated on the PTSC, and concentrated solar irradiance is passed thought the glass cover and is absorbed by absorber tube by radiation ($\dot{Q}_{\text{rad,r-a}}$). Heat exchange among the absorber tube and nanofluid heat transfer in the absorber tube by convection ($\dot{Q}_{\text{conv,a-nf}}$), heat exchange inside the lower part of annulus-air (anna) due to natural convection ($\dot{Q}_{\text{conv,a-anna}}$), heat losses due to radiation of lower part of the absorber tube and glass cover with sky ($\dot{Q}_{\text{rad,g-sky}}$), ($\dot{Q}_{\text{rad,a-sky}}$), heat loss due to conduction of upper part of absorber tube with outside air through the insulation roof ($\dot{Q}_{\text{cond,a-ins}}$), and convection heat losses from glass cover to surrounding ($\dot{Q}_{\text{conv,g-env}}$) are the other heat transferred mechanisms inside the PTSC. Heat losses due to conduction, in the present investigation, through the insulator roof are negligible as this is done in similar investigation [42]. Heat loss to environment happens by radiation and convection heat transfer mechanisms. Type of convection heat transfer is specified by wind conditions. The following assumptions are employed to simplize the simulation [43]:

- The exchange of radiation heat transfer in infrared spectrum amounts to zero.
- The glass cover thickness is very thin in comparison with other dimension, and therefore, the solar irradiance absorptance in glass cover is negligible.

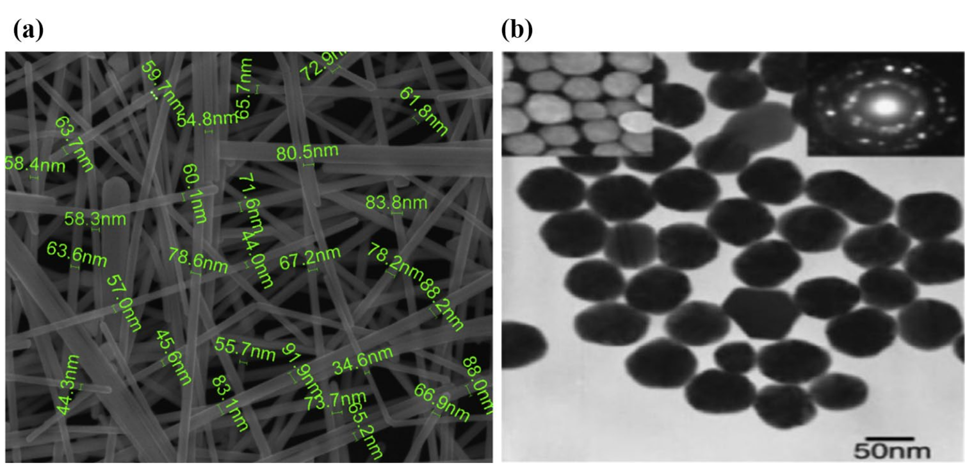

Fig. 7 **a** SEM of the silver nanowire; and **b** TEM of the truncated near-spherical silver particles (d_{np}< 100 nm) [32]

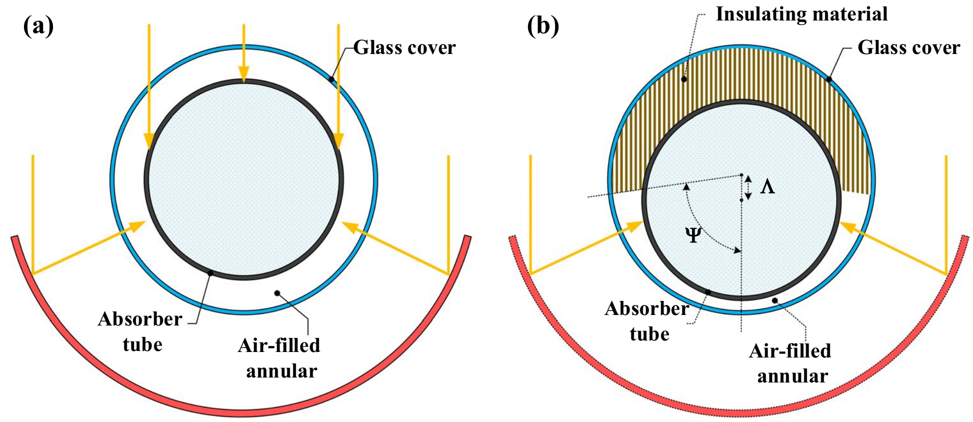

Fig. 8 Schematic diagrams of **a** C.PTSC and **b** N.PTSC

Table 5 Nanoparticle shape effect contribution and surface resistance on the nanoparticle thermal conductivity [14]

Type	Aspect ratio	ψ	C_k	C_k^{shape}	$C_k^{\text{surface}} = C_k - C_k^{\text{shape}}$
Platelets	1:1/8	0.52	2.61	5.72	−3.11
Blades	1:6:1/12	0.36	2.74	8.26	−5.52
Cylindrical	1:8	0.62	3.95	4.82	−0.87
Bricks	1:1:1	0.81	3.37	3.72	−0.35

Table 6 Coefficients of viscosity for various particle shapes at 25 °C [14]

	Blade	Platelet	Brick	Cylindrical
A_1	14.6	37.1	1.9	13.5
A_2	123.3	612.6	471.4	904.4

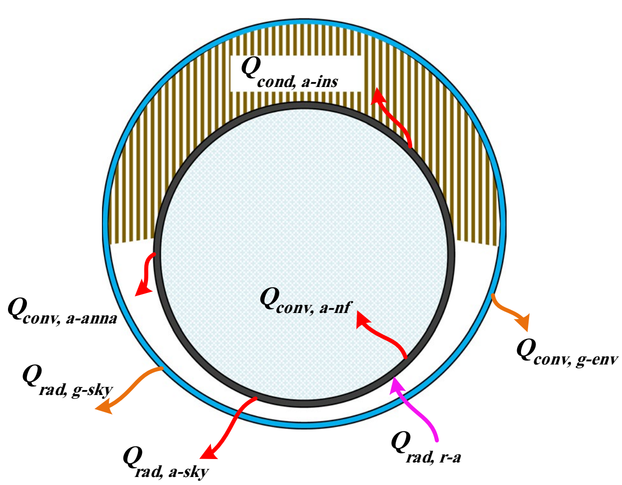

Fig. 9 Schematic of the heat transfer mechanisms of the novel PTSC

- The pressure gradient has been determined low enough to make nanofluid in incompressible and steady-state conditions.
- Different edges are determined in adiabatic adding condition with zero heat loss.
- Air flow in annulus is steady state and incompressible and has laminar regime.

Heat transfer from the insulated section of annulus is given by the following equation [44]:

$$\frac{A}{2}\rho_{\text{nf}}c_{\text{p,nf}}\frac{\mathrm{d}T_{\text{nf}}}{\mathrm{d}t} = -\dot{m}\frac{\mathrm{d}}{\mathrm{d}z}\left(c_{\text{p,nf}}T_{\text{nf}} + \frac{V_{\text{nf}}^2}{2}\right) + Q_{\text{conv,a-nf}}, \quad (13)$$

where $Q_{\text{conv,a-nf}}$ is calculated by Eq. (14) and the Nusselt number is determined with the relation presented by Eqs. (15)–(23) [45, 46]:

$$Q_{\text{conv,a-nf}} = \pi \text{Nu}_{\text{nf}} k_{\text{nf}} \left(T_{\text{a}} - T_{\text{nf}}\right), \quad (14)$$

$$\text{Nu}_{\text{nf}} = \frac{\frac{\mathcal{F}_{\text{ann}}}{8}\text{RePr}}{\mathcal{K} + 12.7\sqrt{\frac{\mathcal{F}_{\text{ann}}}{8}}\left(\text{Pr}^{2/3} - 1\right)}\left(1 + \left(\frac{d_{\text{h}}}{L}\right)^{2/3}\right)\mathbb{F}_{\text{ann}}\mathbb{K}. \quad (15)$$

Different parameters in the above equation are calculated as follows [46]:

$$\mathcal{K} = 1.07 + \frac{900}{\text{Re}} - \frac{0.63}{1 + 10\text{Pr}}, \quad (16)$$

$$\mathcal{F}_{\text{ann}} = \left(1.08\log_{10}\text{Re}^* - 1.5\right)^{-2}, \quad (17)$$

$$\text{Re}^* = \text{Re}\frac{\left(1+\mathcal{D}^2\right)\ln\mathcal{D} + \left(1-\mathcal{D}^2\right)}{\left(1-\mathcal{D}^2\right)\ln\mathcal{D}}, \quad (18)$$

$$\mathcal{D} = \frac{d_{\text{a}}}{d_{\text{g}}}, \quad (19)$$

$$\mathbb{F}_{\text{ann}} = 0.75\mathcal{D}^{-0.17}, \quad (20)$$

$$\text{Re} = \frac{u_m d_{\text{h}}}{\mu_{\text{nf}}}, \quad (21)$$

$$\text{Pr} = \frac{\vartheta_{\text{nf}}}{\alpha_{\text{nf}}}, \quad (22)$$

$$\mathbb{K} = \left(\frac{\text{Pr}}{\text{Pr}_{\text{w}}}\right)^{0.11}, \quad (23)$$

where Pr is the liquid Prandtl number with bulk temperature and Pr_{w} is the liquid Prandtl number with wall temperature, respectively.

Two heat transfer mechanism types from the absorber tube happen, natural convective heat transfer mechanism presented by Eq. (24), and radiation heat exchange mechanism among the absorber tube and glass tube which is estimated with view factors calculation [47].

$$Q_{\text{conv,a-anna}} = h_{\text{a}}\pi d_{\text{a}}\left(T_{\text{a}} - T_{\text{g}}\right). \quad (24)$$

The heat exchange among the glass tube and the surrounding is by radiation and convection mechanisms. Moreover, two conditions for convection heat transfer losses can happen: completely natural convection (for the condition in which the wind velocity is supposed to be zero) or forced convection (for the condition in which the wind velocity is considerable). For the present study, heat losses happen due to convection heat transfer for considerable wind velocity as follows [47, 48].

$$Q_{\text{conv,g-env}} = h_{\text{g}}\pi d_{\text{g}}\left(T_{\text{g}} - T_{\text{env}}\right). \quad (25)$$

The coefficient of convective heat transfer (h_{g}) is determined as [47, 48]:

$$h_{\text{g}} = \frac{\text{Nu}_{\text{g}}k_{\text{g}}}{d_{\text{g}}}, \quad (26)$$

where the average Nusselt number for substantial wind velocity is presented as [49]:

$$\text{Nu}_{\text{g}} = c\text{Re}_D^m\text{Pr}^\eta\left(\frac{\text{Pr}}{\text{Pr}_{\text{w}}}\right)^{\varpi}. \quad (27)$$

The values of m and η proposed for presented equation are provided by [49]. The present value for ϖ related to the heat flux direction: $\varpi = 0.25$ is proposed for fluid heating [44, 49].

2.3 Governing equations

In order to simulate the Syltherm 800 oil/γ-AlOOH nanofluid flow through the PTSC, two techniques are employed in the current investigation. The first one, that is used in the validation case, and for air modeling in annulus, is the SPM (in Sect. 2.5), which presumed that both base fluid (Syltherm 800 oil) and particles (γ-AlOOH) have the same velocity field and temperature. Therefore, the governing equations must be provided as if the nanofluid is a *Newtonian* classical fluid by employing the effective thermophysical properties of final suspension. The second approach is founded on the single fluid TPM [50], supposing that the coupling among the phases is robust, and nanoparticles closely follow the flow of suspension [51]. The two phases (solid and fluid) have been suggested to be inter-penetrating, and it is equivalent to each phase that takes its particular velocity field, and inside each control volume, it is a volume fraction for main phase (fluid) and another volume fraction for the another phase (solid). TPM model is illustrated to give powerful estimations even for low nanoparticle volume fractions [52]. The conservation for momentum, mass and energy for the mixture (nanofluid) is used instead of employing the governing equations of each fluid and solid phases separately [53]. The continuity equation is written as follows:

$$\nabla\left(\rho_m\vec{U}_m\right) = 0, \quad (28)$$

where the mixture velocity or mass-averaged velocity, $\vec{U}_m$, is written as [54]:

$$\vec{U}_m = \frac{\rho_{\text{s}}\phi_{\text{s}}\vec{U}_{\text{s}} + \rho_{\text{bf}}\phi_{\text{bf}}\vec{U}_{\text{bf}}}{\rho_m}, \quad (29)$$

where $\vec{U}_{\text{s}}$ and $\vec{U}_{\text{bf}}$ refer to the velocity of particle and velocity of base fluid, respectively, and ρ_m refers to the density of two-phase mixture which are defined as follows [54]:

$$\rho_m = \rho_s\phi_s + \rho_{bf}\phi_{bf}. \tag{30}$$

The steady-state momentum equation is [54]:

$$\rho_m\left(\vec{U}_m\nabla\vec{U}_m\right) = -\vec{\nabla}p + \mu_m\left(\vec{\nabla}\vec{U}_m + \left(\vec{\nabla}\vec{U}_m\right)^{\mathrm{T}}\right) + \vec{\nabla}\left(\rho_{bf}\phi_{bf}\vec{U}_{dr,bf}\vec{U}_{dr,bf} + \rho_s\phi_s\vec{U}_{dr,s}\vec{U}_{dr,s}\right) + \rho_m\vec{g}, \tag{31}$$

where p and μ_m refer to the pressure and mixture viscosity, respectively, $\vec{U}_{dr,bf}$ and $\vec{U}_{dr,s}$ refer to the particles drift velocity and base fluid drift velocity, respectively [54]:

$$\vec{U}_{dr,bf} = \vec{U}_{bf} - \vec{U}_m, \tag{32}$$

$$\vec{U}_{dr,s} = \vec{U}_s - \vec{U}_m. \tag{33}$$

The steady-state equation for energy is defined as follows [54]:

$$\vec{\nabla}\left(\rho_{bf}\phi_{bf}\vec{U}_{bf}h_{bf} + \rho_s\phi_s\vec{U}_s h_s\right) = \vec{\nabla}\left(\left(\phi_{bf}k_{bf} + \phi_s k_s\right)\vec{\nabla}T\right), \tag{34}$$

where h_{bf} and h_s refer to the base fluid and solid nanoparticles enthalpy, respectively. The two-phase mixture volume fraction equation is as [54]:

$$\nabla\left(\rho_s\phi_s\vec{U}_m\right) = -\vec{\nabla}\left(\rho_s\phi_s\vec{U}_{dr,s}\right). \tag{35}$$

The slip velocity is written as [54]:

$$\vec{U}_{bf,s} = \vec{U}_{bf} - \vec{U}_s, \tag{36}$$

and the relation among the relative velocity and drift velocity is defined as [54]:

$$\vec{U}_{dr,s} = \vec{U}_{s,bf} - \frac{\rho_s\phi_s}{\rho_m}\vec{U}_{bf,s}. \tag{37}$$

The relative velocity is presented by the Schiller and Naumann [55] relation as:

$$\vec{U}_{bf,s} = \frac{d_p^2}{18\mu_{bf}f_d}\frac{\rho_s - \rho_m}{\rho_s}\vec{\alpha}, \tag{38}$$

$$f_d = 1 + 0.15\mathrm{Re}_s^{0.687}, \tag{39}$$

$$\vec{\alpha} = \vec{g} - \left(\vec{U}_m\nabla\vec{U}_m\right), \tag{40}$$

where $\vec{g}$ and $\vec{\alpha}$ refer to the fluid and particle acceleration of gravity, respectively. The Reynolds number (Re_s) of particle is presented as:

$$\mathrm{Re}_s = \frac{d_p\vec{U}_m\rho_m}{\mu_m}, \tag{41}$$

where d_p refers to the mean diameter of particle, here 38 nm.

In all simulated models during the current investigation, the fluid flow of the HTF in the absorber tube is in the turbulent flow regime, since the Reynolds number is higher than 2300 (details in Sect. 2.1). For simulating the turbulent fluid flows in the absorber tube, in addition to the conservation equation for mass, momentum and energy, the turbulent modeling equations must be employed in used commercial software [50]. In the current work, the k–ε turbulent model in employed. The selection of the k–ε turbulent model is according to its common employment, since this is effectively employed in numerous numerical investigations in PTSCs [56–60]. For the HTF, the temperature-dependent thermophysical properties are considered. The k–ε model equations are as follows:

$$\vec{\nabla}\left(\rho_m\vec{U}_m k\right) = \vec{\nabla}\left[\left(\mu_m + \frac{\mu_{t,m}}{\sigma_k}\right)\vec{\nabla}k\right] + G_{k,m} - \rho_m\varepsilon, \tag{42}$$

$$\vec{\nabla}\left(\rho_m\vec{U}_m\varepsilon\right) = \vec{\nabla}\left[\left(\mu_m + \frac{\mu_{t,m}}{\sigma_\varepsilon}\right)\vec{\nabla}\varepsilon\right] + \frac{\varepsilon}{k}\left(c_1G_{k,m} - c_2\rho_m\varepsilon\right), \tag{43}$$

where $\mu_{t,m}$ and G that refer to the turbulent viscosity and production rate of k, respectively, are presented [56–60]:

$$\mu_{t,m} = C_\mu\rho_m\frac{k^2}{\varepsilon}, \tag{44}$$

$$G_{k,m} = \mu_{t,m}\left(\nabla\vec{U}_m + \left(\nabla\vec{U}_m\right)^{\mathrm{T}}\right). \tag{45}$$

The standard constants are employed, $C_\mu = 0.09$, $c_1 = 1.44$, $c_2 = 1.92$, $\sigma_k = 1.00$, $\sigma_\varepsilon = 1.30$ and $\sigma_t = 0.85$.

Radiation modeling inside the annulus has been done with the Monte Carlo approach [50], where the radiation is determined to affect the surface of domain with heating, while it is not radiant energy exchange with the medium (*surface-to-surface*, S2S). This hypothesis is reliable since the space of annulus is considered filled with low-pressure air (lower than 0.83 atm) as already mentioned in Sect. 2.1. Gray model (GM) is employed to model the spectral dependence of the radiative heat exchange equation which considers all radiation magnitudes are unvarying in the spectrum. Steady-state form of the governing equations is utilized with higher-order discretization. The convergence criterion value for the nanofluid flow and heat transfer is to be less than 10^{-6}. For analyzing the fluid (or nanofluid) fluid flow and heat transfer characteristics specifications of various volume fractions in solar receivers, some useful interested parameters are written as follows. Reynolds number of fluid flow is defined as [61, 62]:

$$\mathrm{Re} = \frac{\rho_{\mathrm{bf}} u_m d_{\mathrm{a}}}{\mu_{\mathrm{bf}}}, \tag{46}$$

where u_m refers to the average velocity of fluid through the test section and Nusselt number is calculated as:

$$\mathrm{Nu} = \frac{h_{\mathrm{bf}} d_{\mathrm{a}}}{k_{\mathrm{bf}}}, \tag{47}$$

where k_{bf} and h_{bf} illustrate the fluid thermal conductivity and heat transfer coefficient, respectively.

The pressure drop through the test section is defined as:

$$\Delta p = p_{\mathrm{av,inlet}} - p_{\mathrm{av,outlet}}. \tag{48}$$

The friction factor is calculated as:

$$f = \frac{2}{\left(\frac{L}{d_{\mathrm{a}}}\right)} \frac{\Delta p}{\rho_{\mathrm{nf}} u_m^2}. \tag{49}$$

The performance evaluation criterion (PEC) is utilized for the thermal and fluid performances of solar heat exchanger with nanofluid to estimate the real heat transfer improvement. It is determined employing the calculated friction factor and Nusselt numbers as follows [61, 62]:

$$\mathrm{PEC} = \left(\frac{\mathrm{Nu}_{\mathrm{av}}}{\mathrm{Nu}_{\mathrm{av},0}}\right) \cdot \left(\frac{f}{f_0}\right)^{-1/3}, \tag{50}$$

where $\mathrm{Nu}_{\mathrm{av}}$ and $\mathrm{Nu}_{\mathrm{av},0}$ are the averaged Nusselt number of enhanced PTSC and the averaged Nusselt number of reference PTSC, respectively. On the other side, f and f_0 are the friction factor for enhanced PTSC and the reference PTSC, respectively. In case of a conventional collector, the collector efficiency, η_{c}, as a significant index, reporting the ability of the receiver to change the solar energy into the thermal energy may be assessed by [9]:

$$\eta_{\mathrm{c}} = \frac{E_{\mathrm{c}}}{IA} = \frac{Q_{\mathrm{in}} \rho_{\mathrm{in}} c_{\mathrm{p,in}} \left(T_{\mathrm{out}} - T_{\mathrm{in}}\right)}{6 * 10^4 IA}. \tag{51}$$

Table 7 Grid independence test

No.	Nodes	T_{out} (°C)	Error (%)
1	462,727	84.4579	15.51
2	856,009	71.3579	6.27
3	1,365,347	66.8734	9.27
4	2,124,817	60.6703	3.96
5	2,721,873	58.2745	0.03
6	2,933,289	58.2567	–

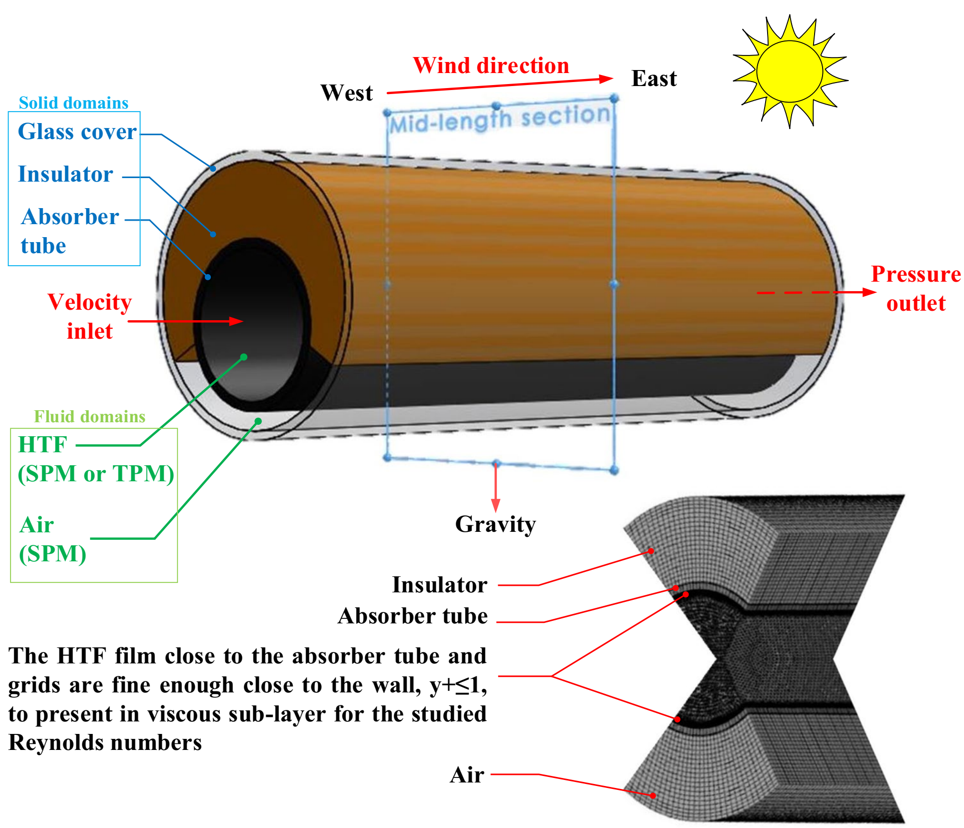

Fig. 10 Schematic diagram of geometry, fluid and solid domains, boundary conditions, wind direction, and schematic diagram of unstructured grid mesh

2.4 Boundary conditions summery

Figure 10 illustrates the boundary conditions, fluid and solid domains, wind direction, schematic diagram geometry (in case of novel PTSC (C.PTSC) with Λ = 15 mm, and Ψ = 50°), and schematic diagram of unstructured grid mesh (in case of conventional PTSC (C.PTSC) with Λ = 0 mm, and Ψ = 90°) in the present study. As it is noted in this figure, the grids in the HTF film near the absorber tube are fine adequate close to the walls ($y+\leq 1$) to present the solution inside the viscous sub-layer for studied Reynolds numbers.

2.5 Validation

As shown in Table 7, a grid independence check was made for the conventional collector using water to examine the influence of grid sizes on the numerical results. As it is seen, six sets of mesh are generated and tested. By comparing the results, it is concluded that mesh configuration that contains grid number of 2,933,289 nodes is assumed to get a satisfactory agreement among the time of computation and the accuracy of results with the maximum error of 0.03%.

Also, CFD code validation was accomplished by comparing the numerical results achieved from the present study (with SPM and TPM) and experimental data of Dudley et al. [38] and also numerical results of Kaloudis et al. [34] (with TPM) with identical dimension and boundary condition with nanofluid. These compressions are presented in Fig. 11. It is concluded from the present figure that a notable proximity exists among the Dudley et al. [38] empirical data, numerical results of Kaloudis et al. [34] and numerical results achieved from the present study with SPM and TPM. It is seen that the TPM simulation in the present work leads to a better validation with experimental data.

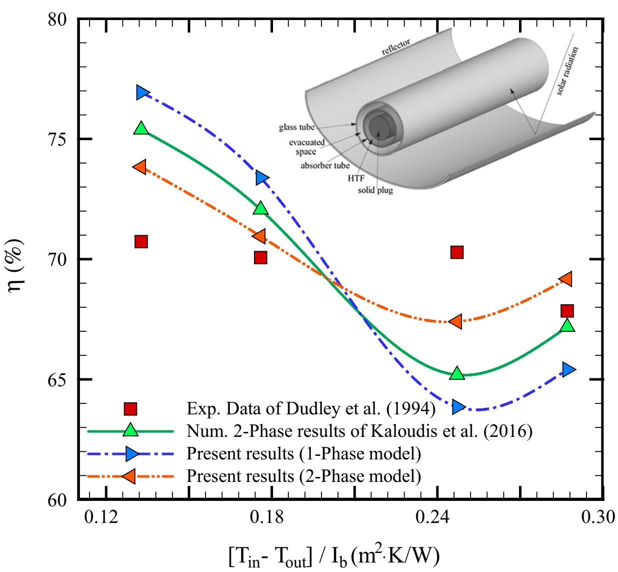

Fig. 11 Code validation among the present work results (with single- and two-phase mixture models), experimental data of Dudley et al. [38] and numerical results of Kaloudis et al. [34]

3 Results and discussion

In the first step of this section, the difference between the SPM and TPM simulations results is investigated for N.PTSC. In the next step, the optimum nanoparticles volume fraction and diameter for spherical morphology are introduced. And finally, the non-spherical morphologies are analyzed. As it was noted previously, in order to simulate the nanofluid flow in PTSCs during the current study, two simulation approaches are used. The first one is the SPM and the second technique is TPM. One of the goals of the present work is to compare the SPM and TPM simulation results in terms of using different nanoparticles morphologies in PTSCs. Therefore, the HTF which is flowed in absorber tube is simulated with the SPM and TPM approaches. The air in annulus for all studied cases in the present work is simulated with the SPM.

3.1 Comparison between the single- and two-phase mixture models

Figure 12 demonstrates the temperature distribution and streamlines in the mid-length cross section of N.PTSC filled with the nanofluid for ϕ = 4% and Re = 6001.2. The temperature distribution in the annulus-air zone and insulting zone presents that the TPM shows more air temperature than that the SPM. Furthermore, the temperature distribution in the absorber tube zone and HTF zone indicates that the TPM also illustrates more HTF and tube temperature than that the SPM. But, the streamlines in the insulated-annulus-air zone show that both the SPM and TPM present almost the same results in terms of flow velocity.

As it is seen in Fig. 12, the pure natural convection patterns are observed for both method (SPM and TPM), where a large eddy exists in middle of the annulus zone. Figure 13a demonstrates the isotherm lines for the SPM and TPM methods, in the mid-length cross section of the N.PTSC filled with the nanofluid for ϕ = 4% and Re = 6001.2. As it is seen in this figure, the temperature close to the bottom wall is more than that of the higher walls. This behavior is because of more nanoparticles concentration near the bottom wall. Figure 13b illustrates the nanoparticles distribution for the SPM and TPM methods, in the mid-length cross section of the N.PTSC filled with the nanofluid for ϕ = 4% and Re = 6001.2. As it is seen in this figure, the nanoparticles have a non-uniform distribution at the mid-length cross section of the C.PTSC, and the nanoparticles concentrate

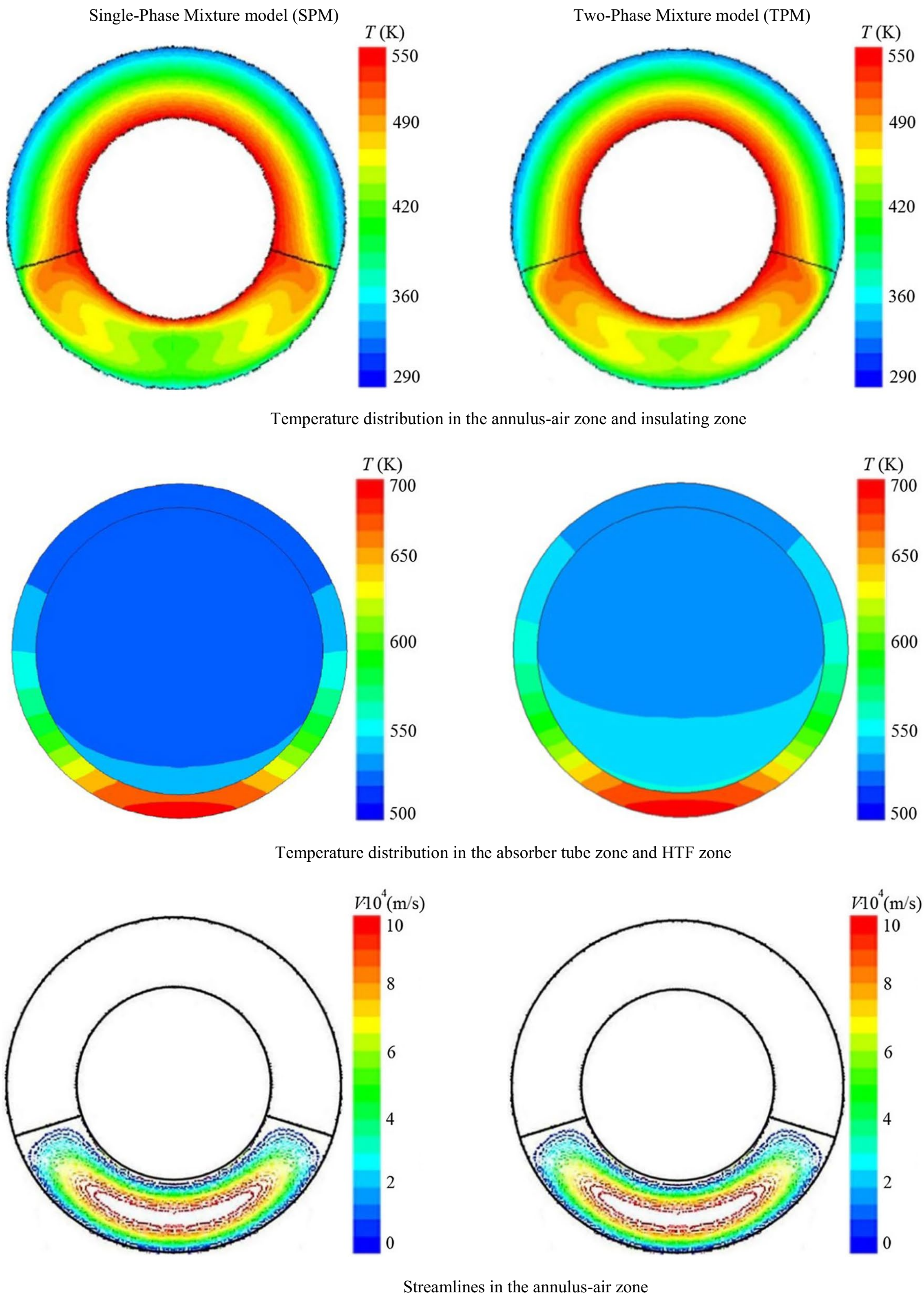

Fig. 12 Temperature distribution and streamlines in the mid-length cross section of N.PTSC filled with the nanofluid at $\phi = 1\%$, Re = 2985.9, $\Lambda = 0$ mm, and $\Psi = 70°$

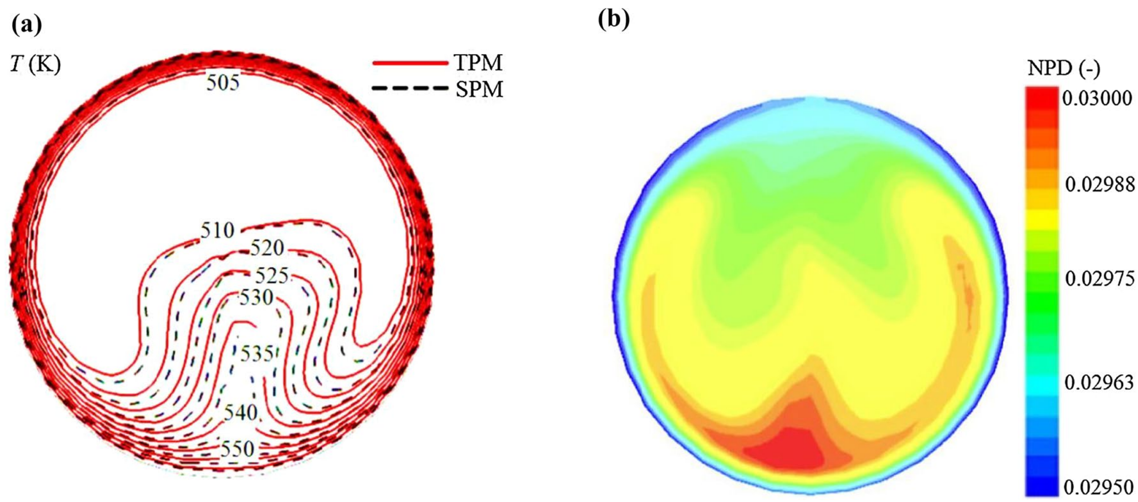

Fig. 13 **a** Isotherm lines for the SPM and TPM models, and **b** nanoparticles distribution for the TPM model, in the mid-length cross section of N.PTSC filled with the nanofluid at $\phi = 1\%$, Re = 2985.9, $\Lambda = 0$ mm, and $\Psi = 90°$

adjacent to the bottom wall due to gravity force. It is clear that the more nanoparticles concentration adjacent to the bottom wall causes higher thermal conductivity of nanofluid in region close to the bottom wall and consequently more heat transfer and temperature values in this region.

Figure 14 illustrates the effects of using the SPM and TPM on the pressure drop, variation of Nusselt number, friction factor, PEC, outlet temperature, and collector efficiency versus Reynolds number in the case of using C.PTSC and N.PTSC ($\Lambda = 0$ mm, and $\Psi = 90°$) filled with the nanofluid ($\phi = 1\%$ and $d_{np} = 20$ mm). As it is shown in Fig. 14a, with the Reynolds number augmentation, the Nusselt number increases also for all studied cases. The higher Reynolds number is related to the greater velocity which can cause the better disturbing of the fluid flow and therefore, the heat transfer is enhanced. It is seen that for both C.PTSC and N.PTSC configurations, the obtained Nusselt number from the TPM simulation is more than that the SPM simulation.

Also it is found that usage of N.PTSC leads to the higher Nusselt number for studied Reynolds numbers and this behavior is due to the lower heat loss in the N.PTSC than that the C.PTSC.

It is clear that using of N.PTSC instead of C.PTSC can increase the average Nusselt number for Re = 11,151.6 about 51%. The minimum differences between the SPM and TPM results in Fig. 14a are 4.82% and 5.04%, respectively.

As it is presented in Fig. 14b, it is shown that the pressure drop of nanofluid flow between inlet and outlet sections of the absorber tube for both the C.PTSC and N.PTSC configurations has the same values. It is clear that this behavior is because of similar inlet wall geometry for both configurations. But also it is seen that the TPM leads to the more pressure drop values at studied Reynolds numbers. Also, the pressure drop increases abruptly with increasing the Reynolds number, and the reason for higher pressure drop at higher Reynolds is the producing stronger vortexes in nanofluid flow at greater Reynolds numbers. The minimum differences between the SPM and TPM results in Fig. 14b are 4.78% and 4.97%, respectively. Figure 14c shows that the nanofluid friction factor always reduces by growing of Reynolds number. Furthermore, the friction factor inside the absorber tube for both C.PTSC and N.PTSC configurations has the same values. It is clear that this behavior is because of similar inlet wall geometry for the both configurations. But also it is seen that the TPM leads to the more friction factor values at all studied Reynolds numbers. The minimum differences between the SPM and TPM results in Fig. 14c are 4.91% and 5.01%, respectively. Figure 14d depicts that for N.PTSC the values of PEC always increase inside the whole studied Reynolds number, which states that maximum Reynolds number (Re = 11,151.6) corresponds to the highest PEC.

The optimum Reynolds number corresponds to Re = 11,151.6. It is seen that the TPM leads to the more PEC values. The PEC of nanofluid flow for Re = 11,151.6 is shown to be the highest between all configurations for studied Reynolds number and is about 1.51. The minimum differences between the SPM and TPM results in Fig. 14d are 4.93% and 5.05%, respectively. As it is shown in Fig. 14e, with the Reynolds number augmentation, the nanofluid outlet temperature also increases for all studied cases. The higher Reynolds number is related to the greater velocity which can cause the better disturbing of the flow and therefore, the heat transfer is enhanced and finally the outlet temperature increased. It is seen that for both C.PTSC and N.PTSC configurations, the obtained

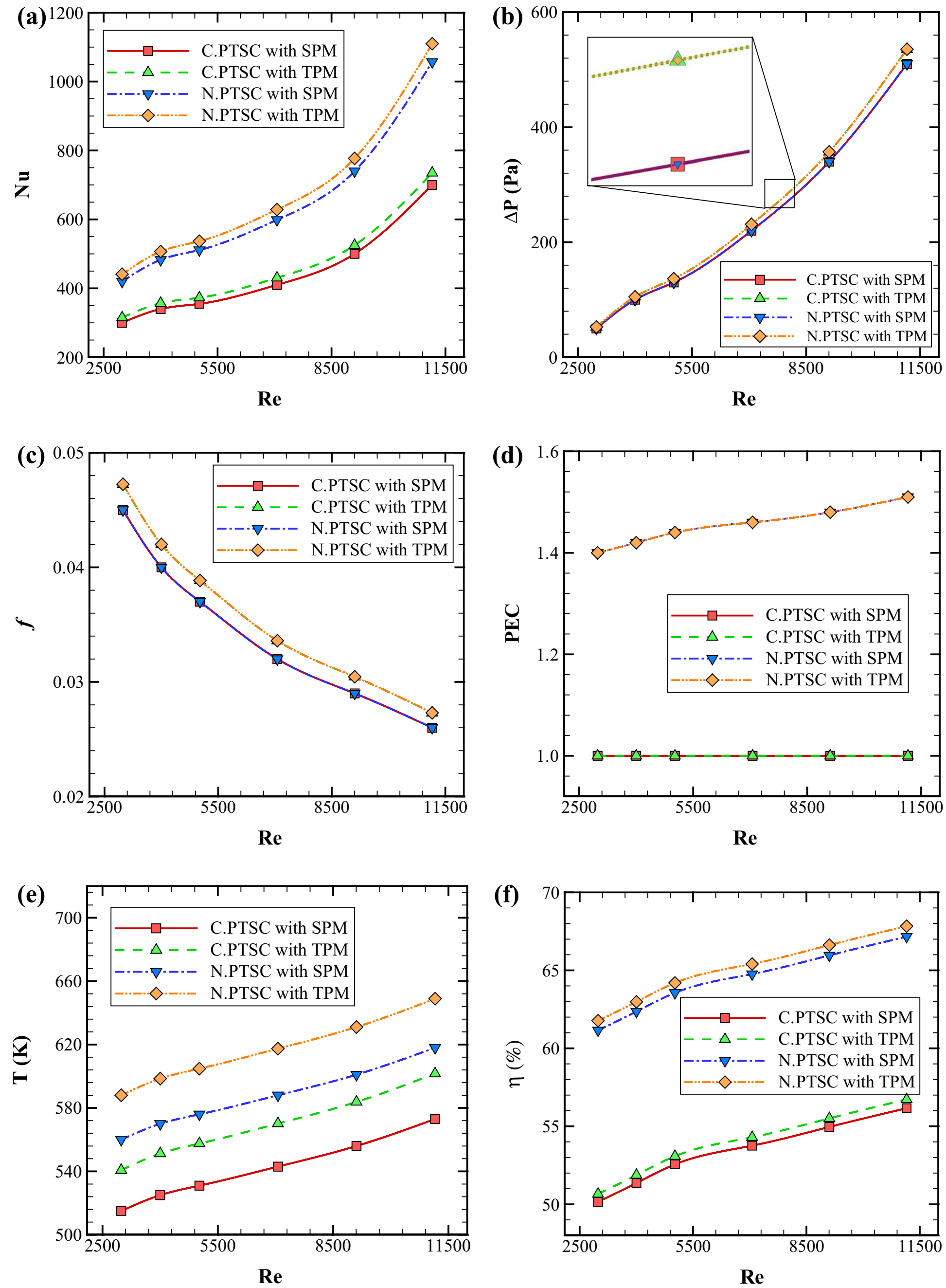

Fig. 14 Effects of using the SPM and TPM on variation of **a** average Nusselt number, **b** pressure drop, **c** friction factor, **d** PEC, **e** outlet temperature and **f** collector efficiency versus Reynolds number in case of using C.PTSC and N.PTSC (Λ = 0 mm, and Ψ = 90°) filled with nanofluid (ϕ = 1% and d_{np} = 20 mm)

outlet temperature from the TPM simulation is more than that of the SPM simulation. Also it is found that employing the N.PTSC leads to the higher outlet temperature at all Reynolds numbers, and this behavior is because of the lower heat loss in N.PTSC than that of C.PTSC. It is clear that using the N.PTSC instead of C.PTSC can increase the outlet temperature for Re = 11,151.6 about 8%. The minimum differences between the SPM and TPM results in Fig. 14e are 4.77% and 4.91%, respectively. As it is presented in Fig. 14f, with the Reynolds number augmentation, the energy efficiency of PTSC increases also for all studied cases. The higher Reynolds number is related to the greater velocity which can cause the better disturbing of the fluid flow and thus, the heat transfer is enhanced and finally the energy efficiency increased. It is seen that, for both C.PTSC and N.PTSC configurations, obtained energy efficiency from the TPM simulation are more than that of the SPM simulation. Also it is found that using the N.PTSC leads to the higher energy efficiency at all Reynolds numbers. It is clear that employing the N.PTSC instead of C.PTSC can increase the energy efficiency for Re = 11,151.6 about 20%. The minimum differences

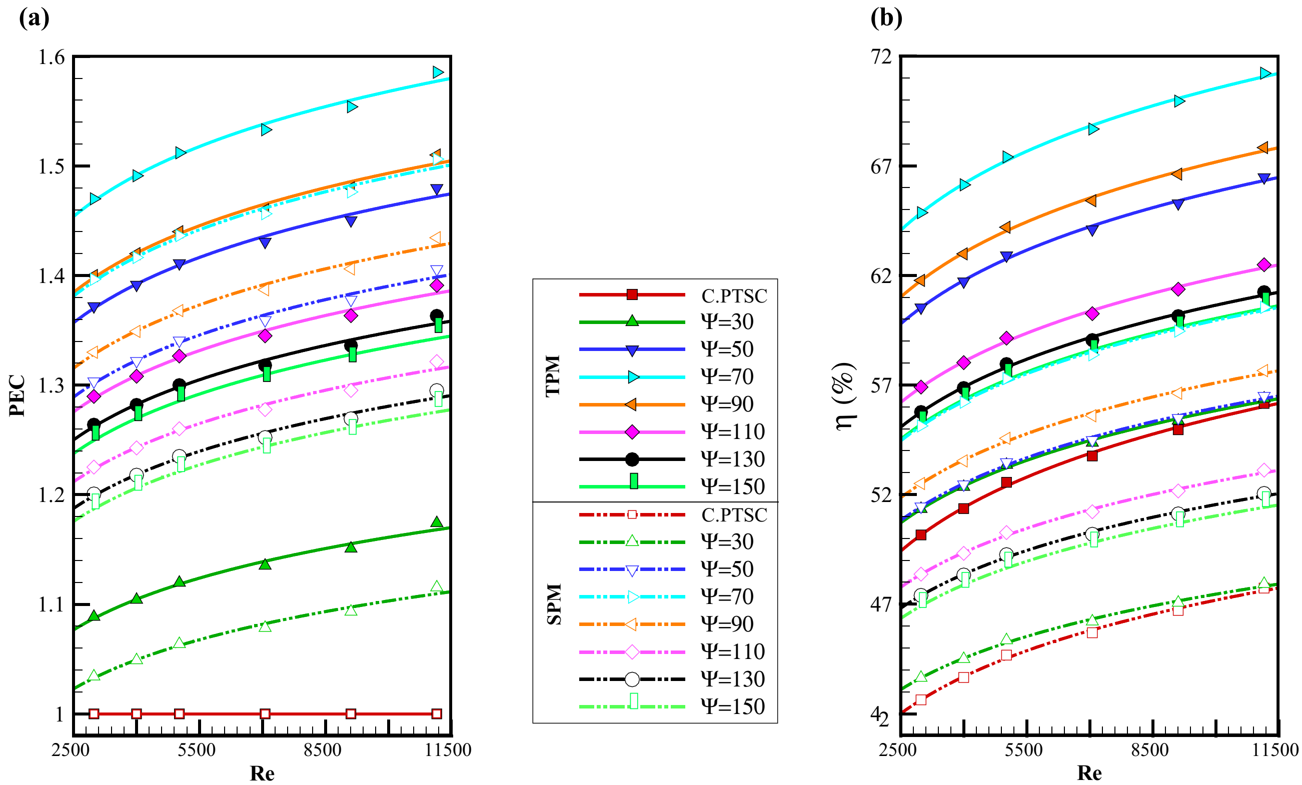

Fig. 15 Effects of different insulator arc-angles on variation of **a** PEC and **b** collector efficiency versus Reynolds number in case of using N.PTSC (Λ = 0 mm) filled with nanofluid (ϕ = 1% and d_{np} = 20 mm)

between the SPM and TPM results in Fig. 14f are 4.85% and 5.00%, respectively. It is clear that the TPM leads to more validated results in comparison with SPM.

3.2 Geometry optimization of N.PTSC

Figure 15 illustrates the effects of different insulator arc-angles on the PEC and collector efficiency versus Reynolds number in case of using N.PTSC ($\Lambda = 0$ mm) filled with nanofluid ($\phi = 1\%$ and $d_{np} = 20$ mm). Figure 15a depicts that the PEC values for all configurations always increase by increasing Reynolds number, which means that the maximum Reynolds number (Re = 11,151.6) corresponds to the maximum PEC. Also, it is realized that for all studied configurations, employing the TPM leads to the more PEC values than that of the SPM. The optimum configuration is related to $\Psi = 70°$ which is followed by $\Psi = 90°, 50°, 110°, 130°, 150°$ and $30°$, respectively, for studied Reynolds numbers. As it is shown in Fig. 15b, with the Reynolds number augmentation, the energy efficiency of PTSC increases also for all investigated configurations. It is shown for both C.PTSC and N.PTSC configurations, the optimum Reynolds number is Re = 11,151.6. Also it is found that the maximum energy efficiency is related to $\Psi = 70°$ which is followed by $\Psi = 90°, 50°, 110°, 130°, 150°$ and $30°$, respectively, for all studied Reynolds numbers. Therefore, in the rest of this study the N.PTSC with $\Psi = 70°$ is employed to analyze the different parameters. Also, it is found that for all investigated models, employing the TPM leads to the higher energy efficiency than that of the SPM.

Figure 16 illustrates the effects of different acentric values on the PEC and collector efficiency versus Reynolds number in the case of using N.PTSC ($\Psi = 70°$) filled with nanofluid ($\phi = 1\%$ and $d_{np} = 20$ mm). Figure 16a depicts that the PEC values for all configurations always increase by increasing of Reynolds number, which means that the maximum Reynolds number (Re = 11,151.6) corresponds to the maximum PEC.

Also, it is realized that for all studied configurations, employing the TPM leads to the more PEC values than that the SPM. The optimum configuration is related to acentric value of $\Lambda = 20$ mm has the maximum Nusselt number among all configurations, which is followed by $\Lambda = 15, 10, 5$ and 0 mm, respectively, for considered Reynolds numbers. As it is shown in Fig. 16b, with the Reynolds number augmentation, the energy efficiency of PTSC increases also for all studied configurations.

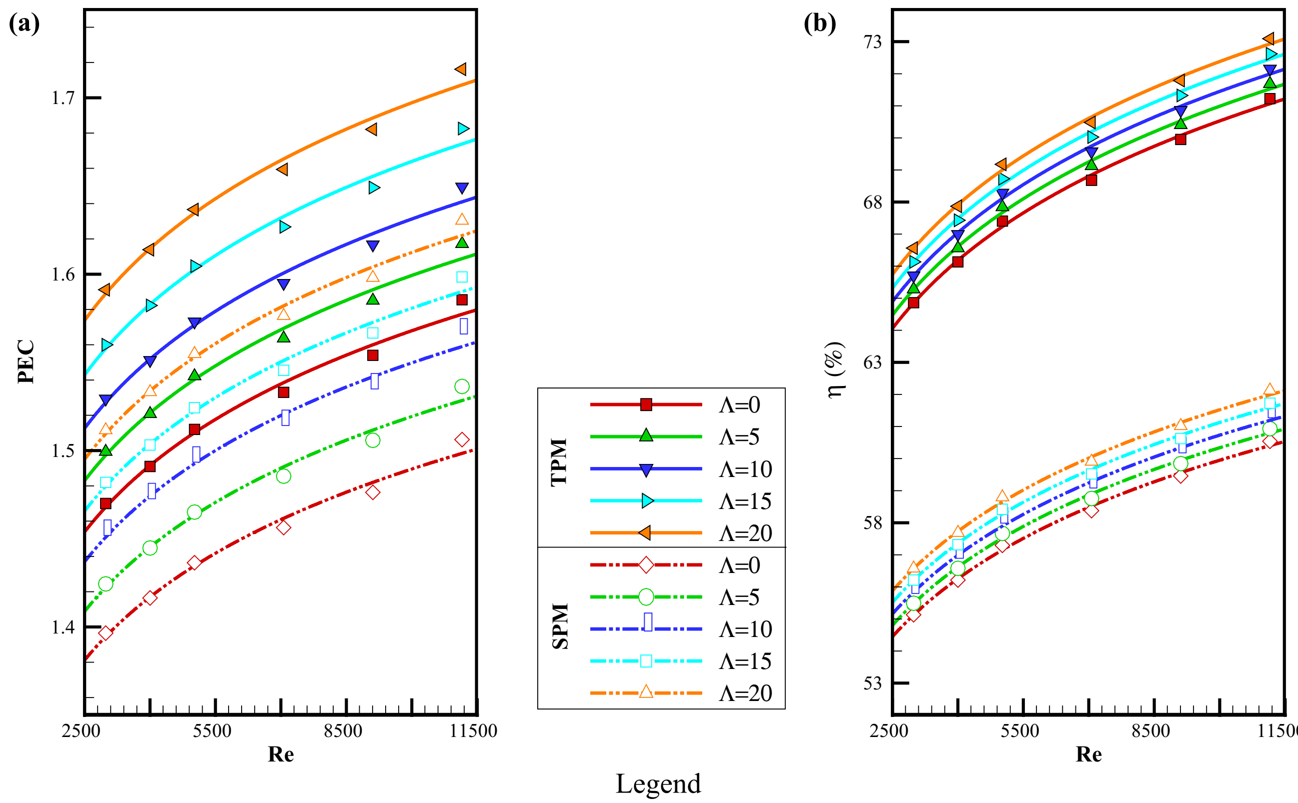

Fig. 16 Effects of different acentric values on variation of **a** PEC and **b** collector efficiency versus Reynolds number in case of using N.PTSC (Ψ = 70°) filled with nanofluid (ϕ = 1% and d_{np} = 20 mm)

3.3 Nanofluid details

Figure 17 illustrates the effects of different nanoparticles volume fractions on PEC and collector efficiency versus Reynolds number in case of using N.PTSC (Ψ = 70° and Λ = 20 mm) filled with nanofluid (d_{np} = 20 mm).

Figure 17a depicts that the PEC values for all cases always increase by augmentation of Reynolds number and reduction of nanoparticle volume fraction, which shows that an optimum Reynolds number (Re = 11,151.6) corresponds to the highest PEC. The optimum case is associated with volume fraction of ϕ = 1%, which is followed by ϕ = 3, 2 and 1%, respectively. Also, it is realized that for all studied configurations, employing the TPM leads to more PEC values than that of the SPM. As it is shown in Fig. 17b, with the Reynolds number augmentation or nanoparticle volume fraction reduction, the energy efficiency of PTSC increases for all studied cases. Therefore, the optimum Reynolds number is Re = 11,151.6 and the optimum nanoparticle volume fraction is ϕ = 1%. The energy efficiency of N.PTSC (Ψ = 70° and Λ = 20 mm) filled with nanofluid (d_{np} = 20 mm) for ϕ = 1% is about 73.10%.

Therefore, in the rest of this study the N.PTSC with Ψ = 70° and Λ = 20 mm filled with nanofluid of ϕ = 1% is analyzed to study the different particle diameters effect. Also, it is found that for all studied configurations, employing the TPM leads to the higher energy efficiency values than that of the SPM.

Figure 18 illustrates the effects of different nanoparticles diameters on the PEC and collector efficiency versus Reynolds number in case of using N.PTSC (Ψ = 70° and Λ = 20 mm) filled with nanofluid (ϕ = 1%) simulated with the TPM. Figure 18a depicts that the PEC values for all cases always increase by increasing of Reynolds number and reduction of nanoparticle diameter, which means that the maximum Reynolds number (Re = 11,151.6) corresponds to the highest PEC. The optimum case is associated with nanoparticles diameter of d_{np} = 20 nm, which is followed by d_{np} = 30, 40, 50 and 60 nm, respectively. Also, it is realized that for all studied configurations, employing the TPM leads to higher PEC values than that of the SPM.

As it is shown in Fig. 18b, with the Reynolds number augmentation or nanoparticle diameter reduction the energy efficiency of PTSC increases for all studied cases. Therefore, the optimum Reynolds number is Re = 11,151.6 and the optimum nanoparticle diameter is d_{np} = 20 nm. The energy

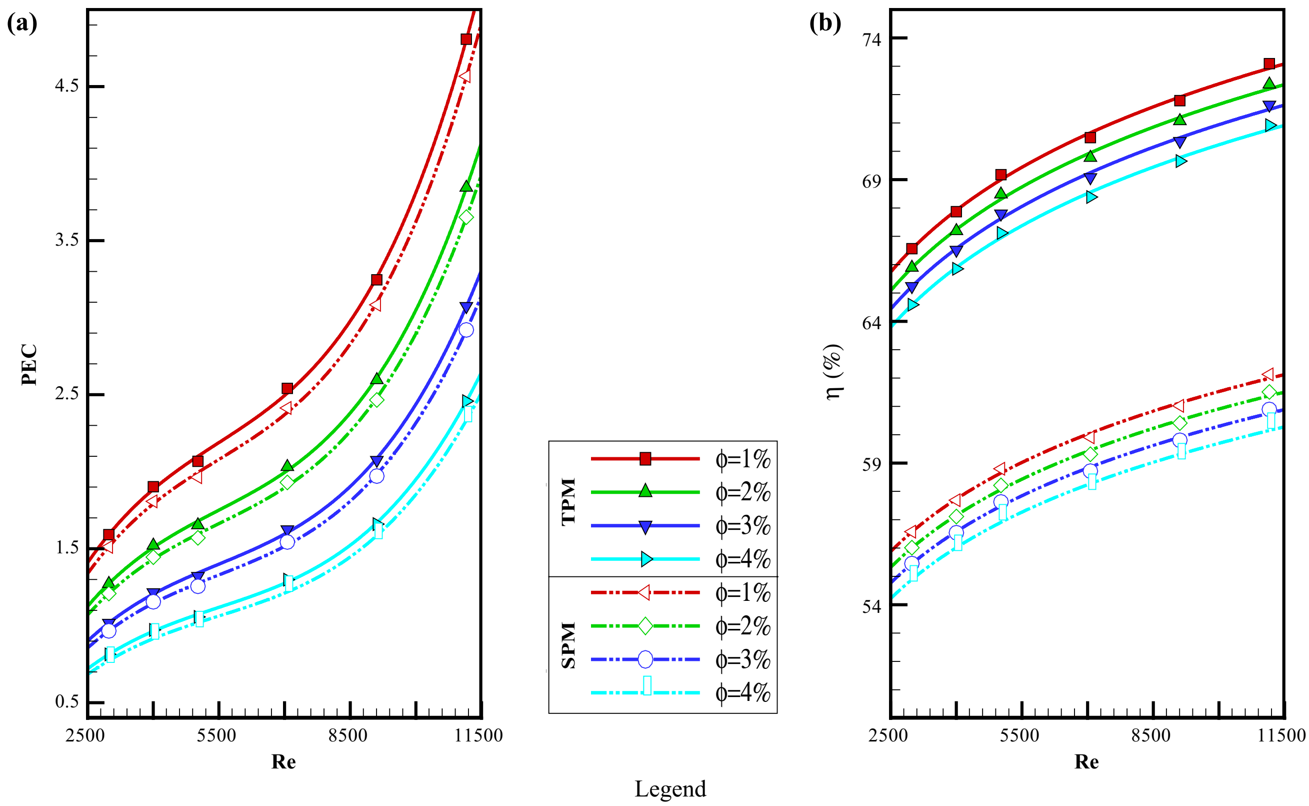

Fig. 17 Effects of different nanoparticles volume fractions on variation of **a** PEC and **b** collector efficiency versus Reynolds number in case of using N.PTSC (Ψ = 70° and Λ = 20 mm) filled with nanofluid (d_{np} = 20 mm)

efficiency of N.PTSC (Ψ = 70° and Λ = 20 mm) filled with nanofluid of d_{np} = 20 mm and ϕ = 1% is about 73.10% and is the maximum obtained energy efficiency in present study. Also, it is found that for all investigated models, employing the TPM leads to higher energy efficiency values than that of the SPM.

Figure 19 illustrates the effects of different nanoparticles shapes on the PEC and collector efficiency versus Reynolds number in case of using N.PTSC (Ψ = 70° and Λ = 20 mm) filled with nanofluid (ϕ = 1% and d_{np} = 20 mm). Figure 19a depicts that the PEC values for all cases always increase till Re = 5000 and then reduce and again increase till Re = 11,151.6 by increasing of Reynolds number, which shows that the maximum Reynolds number (Re = 11,151.6) corresponds to the highest PEC. The optimum case is associated with the nanoparticles shape of blade which is followed by brick, cylinders and platelet, respectively. Also, it is realized that for all studied configurations, employing the TPM leads to the higher PEC values than that of the SPM. As it is shown in Fig. 19b, with the Reynolds number augmentations, the energy efficiency of PTSC increases for all studied cases till Re = 5000 and then always reduces. Therefore, the optimum Reynolds number is Re = 5000. The optimum case is related to the nanoparticles shape of blades which is followed by bricks, cylinders and platelets, respectively. Also, it is found that for all studied configurations, employing the TPM leads to higher energy efficiency values than that the SPM. Their trend is not completely similar with each other.

4 Conclusion

For simulating the nanofluid flow, two approaches are employed in the current study. The first one, employed for validation case and for air modeling in the annulus, is the single-phase mixture model (SPM) and thus governing equations of momentum, energy and mass be employed for the classical Newtonian nanofluid (fluid) by means of effective thermal properties for the fluid and

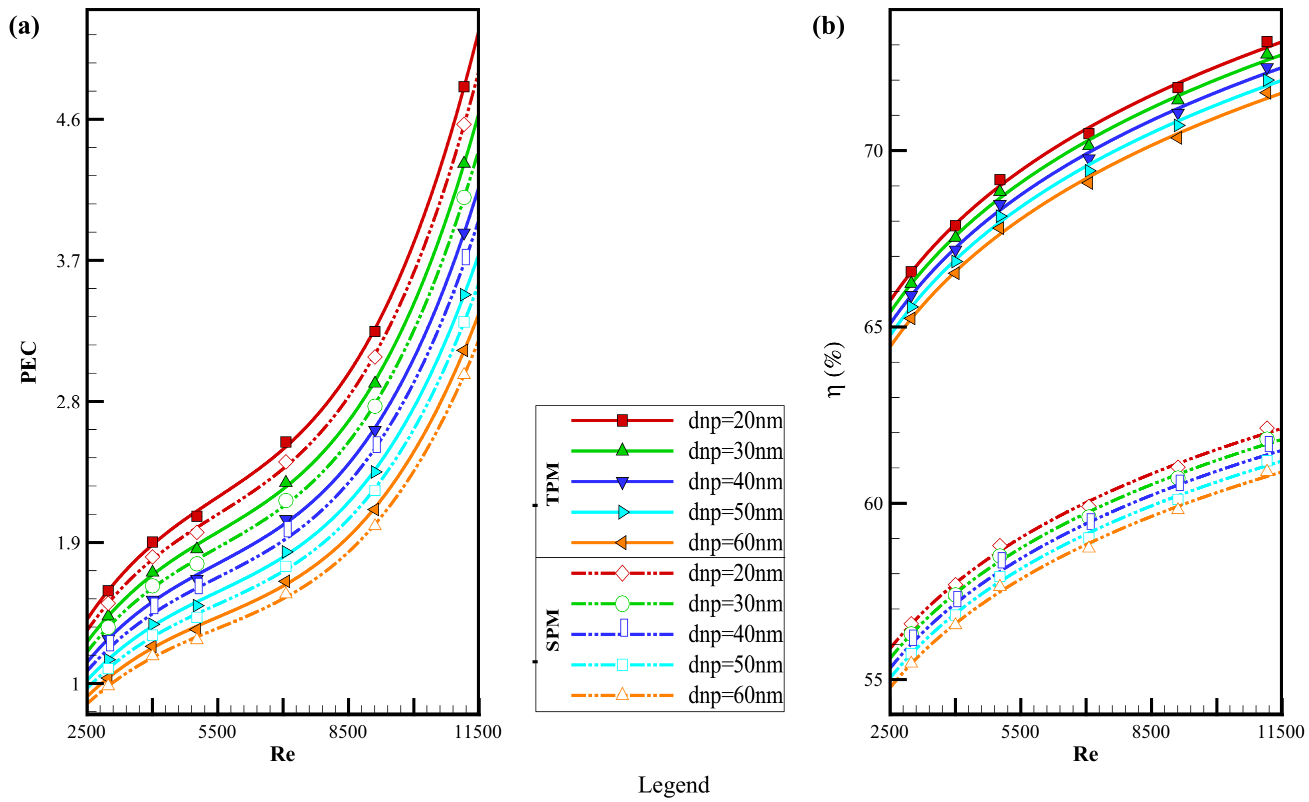

Fig. 18 Effects of different nanoparticles diameters on variation of **a** PEC and **b** collector efficiency versus Reynolds number in case of using N.PTSC (Ψ = 70° and Λ = 20 mm) filled with nanofluid (ϕ = 1%)

nanofluid. And the second approach is constructed on the Eulerian–Eulerian single fluid, two-phase mixture model (TPM). The main objective of the present work was to study the morphology effects of Syltherm 800 oil-based γ-AlOOH nanofluid flow on the thermal–hydraulic performances and energy efficiency of a novel parabolic trough solar collector (N.PTSC) numerically using finite volume method. And the other goal was to compare the obtained numerical results of simulating nanofluid in PTSC using the SPM and TPM. Based on obtained results:

- For all studied cases, the obtained PEC and energy efficiencies from the TPM approach are more than that of SPM approach.
- Using N.PTSC leads to the higher average Nusselt number, energy efficiency, performance evaluation criteria (PEC) and outlet temperature at all Reynolds numbers.
- The configuration with Ψ = 70° has the maximum Nusselt number among all configurations, which is followed by Ψ = 90°, 50°, 110°, 130°, 150° and 30°, respectively.
- The configuration with acentric value of Λ = 20 mm has the maximum Nusselt number among all configurations, which is followed by Λ = 15, 10, 5 and 0 mm, respectively.
- For all cases always the PEC and energy efficiency increase by reduction of nanoparticle volume fraction and diameter.
- The PEC values for all cases always increase till Re = 5000 and then reduce and again increase till Re = 11,151.6 by increasing Reynolds number, which shows that the maximum Reynolds number (Re = 11,151.6) corresponds to the highest PEC.
- As the Reynolds number increases, the energy efficiency of PTSC increases for all studied cases till Re = 5000 and then always reduces. Therefore, the optimum Reynolds number is Re = 5000.
- The optimum morphology is related to the nanoparticles shape of blades which is followed by brick, cylinders and platelet, respectively.

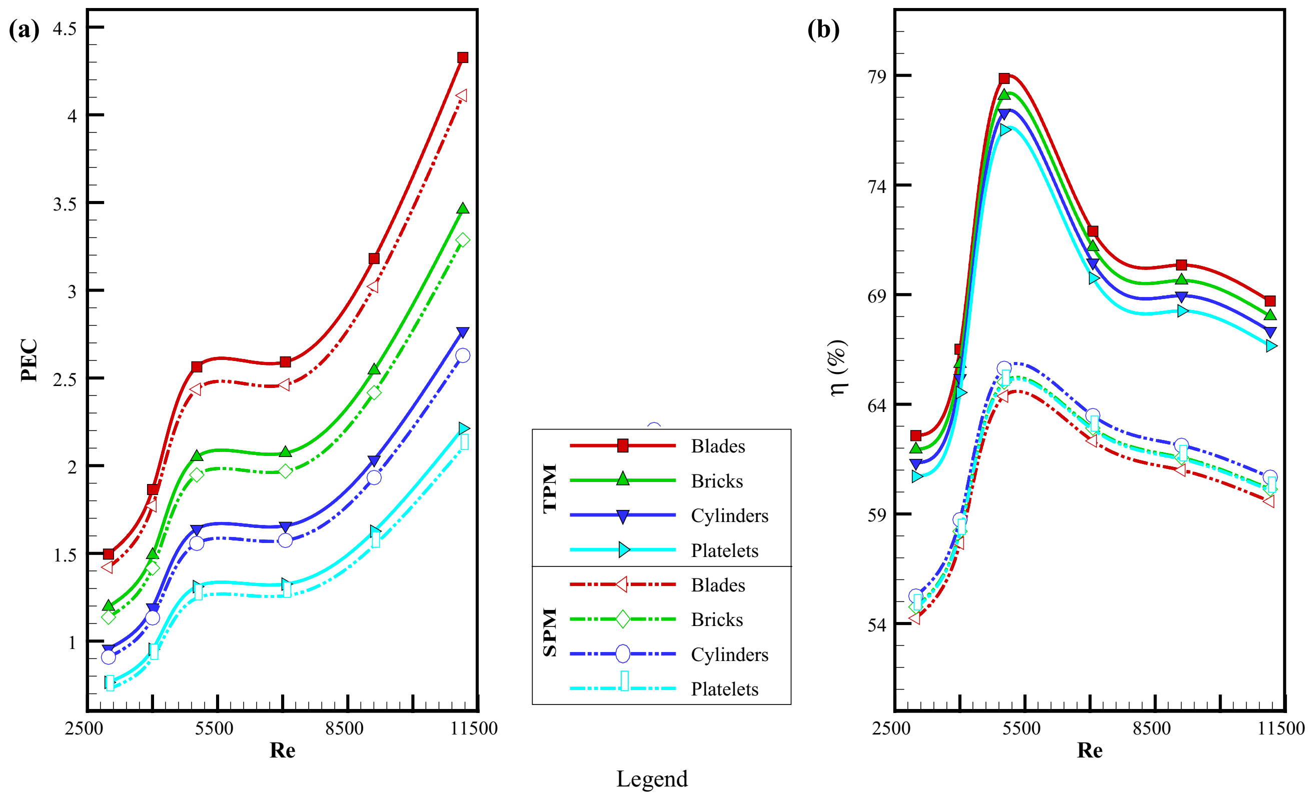

Fig. 19 Effects of different nanoparticles shapes on variation of **a** PEC and **b** collector efficiency versus Reynolds number in case of using N.PTSC (Ψ = 70° and Λ = 20 mm) filled with nanofluid (ϕ = 1% and d_{np} = 20 mm)

References

1. Salgado Conrado L, Rodriguez-Pulido A, Calderon G (2017) Thermal performance of parabolic trough solar collectors. Renew Sustain Energy Rev 67:1345–1359
2. Fuqiang W, Ziming C, Jianyu T, Yuan Y, Yong S, Linhua L (2017) Progress in concentrated solar power technology with parabolic trough collector system: a comprehensive review. Renew Sustain Energy Rev 79:1314–1328
3. Bellos E, Tzivanidis C, Daniil I (2017) Energetic and exergetic investigation of a parabolic trough collector with internal fins operating with carbon dioxide. Int J Energy Environ Eng 8:109–122
4. Bellos E, Tzivanidis C (2018) Assessment of the thermal enhancement methods in parabolic trough collectors. Int J Energy Environ Eng 9:59–70
5. Suman S, Khan MK, Pathak M (2015) Performance enhancement of solar collectors a review. Renew Sustain Energy Rev 49:192–210
6. Lei D, Ren Y, Wang Z (2020) Numerical study of conduction and radiation heat losses from vacuum annulus in parabolic trough receivers. Front Energy. https://doi.org/10.1007/s11708-020-0670-7
7. Aldulaimi RKM (2019) An innovative receiver design for a parabolic trough solar collector using overlapped and reverse flow: an experimental study. Arab J Sci Eng 44:7529–7539
8. Soudani ME, Aiadi KE, Bechki D, Chihi S (2017) Experimental and theoretical study of parabolic trough collector (PTC) with a flat glass cover in the region of algerian sahara (Ouargla). J Mech Sci Technol 31:4003–4009
9. Daffie JA, Beckman WA (2009) Solar engineering of thermal progress, 4th edn. Wiley, New York
10. Wang Q, Li J, Yang H, Su K, Hu M, Pei G (2017) Performance analysis on a high temperature solar evacuated receiver with an inner radiation shield. Energy 139:447–458
11. Khan MS, Yan M, Ali HM, Amber KP, Bashir MA, Akbar B, Javed S (2020) Comparative performance assessment of different absorber tube geometries for parabolic trough solar collector using nanofluid. J Therm Anal Calorim. https://doi.org/10.1007/s10973-020-09590-2
12. Mohamed MH, El-Sayed AZ, Megalla KF, Elattar HF (2019) Modeling and performance study of a parabolic trough solar power plant using molten salt storage tank in Egypt: effects of plant site location. Energy Syst 10:1043–1070
13. Al-Aboosi FY (2020) Models and hierarchical methodologies for evaluating solar energy availability under different sky conditions toward enhancing concentrating solar collectors use: Texas as a case study. Int J Energy Environ Eng 11:177–205
14. Timofeeva EV, Routbort JL, Singh D (2009) Particle shape effects on thermophysical properties of alumina nanofluids. J Appl Phys 106:014304
15. Abbasian Arani AA, Sadripour S, Kermani S (2017) Nanoparticle shape effects on thermal-hydraulic performance of boehmite alumina nanofluids in a sinusoidal–wavy mini-channel with phase shift and variable wavelength. Int J Mech Sci 128–129:550–563

16. Vanaki SM, Mohammed HA, Abdollahi A, Wahid MA (2014) Effect of nanoparticle shapes on the heat transfer enhancement in a wavy channel with different phase shifts. J Mol Liq 196:32–42
17. Mahian O, Kianifar A, Heris SZ, Wongwises S (2014) First and second laws analysis of a minichannel-based solar collector using boehmite alumina nanofluids: effects of nanoparticle shape and tube materials. Int J Heat Mass Transf 78:1166–1176
18. Ooi EH, Popov V (2013) Numerical study of influence of nanoparticle shape on the natural convection in Cu–water nanofluid. Int J Therm Sci 65:178–188
19. Elias MM, Miqdad M, Mahbubul IM, Saidur R, Kamalisarvestani M, Sohel MR, Hepbasli A, Rahim NA, Amalina MA (2013) Effect of nanoparticle shape on the heat transfer and thermodynamic performance of a shell and tube heat exchanger. Int Commun Heat Mass Transf 44:93–99
20. Elias MM, Shahrul IM, Mahbubul IM, Saidur R, Rahim NA (2014) Effect of different nanoparticle shapes on shell and tube heat exchanger using different baffle angles and operated with nanofluid. Int J Heat Mass Transf 70:289–297
21. Khan I (2017) Shape effects of MoS_2 nanoparticles on MHD slip flow of molybdenum disulphide nanofluid in a porous medium. J Mol Liq 233:442–451
22. Hajabdollahi H, Hajabdollahi Z (2017) Numerical study on impact behavior of nanoparticle shapes on the performance improvement of shell and tube heat exchanger. Chem Eng Res Des 125:449–460
23. Avella M, Cosco S, Di Lorenzo ML, Di Pace E, Errico ME (2005) Influence of $CaCO_3$ nanoparticles shape on thermal and crystallization behavior of isotactic polypropylene based nanocomposites. J Therm Anal Calorim 80:131–136
24. Fang X, Ding Q, Fan LW, Yu ZT (2013) Enhanced thermal conductivity of ethylene glycol-based suspensions in the presence of silver nanoparticles of various sizes and shapes. In: Proceedings of the ASME 2013 heat transfer summer conference, HT2013, July 2013, Minneapolis, MN, USA, pp 14–19
25. Ferrouillat S, Bontemps A, Poncelet O, Soriano O, Gruss JA (2013) Influence of nanoparticle shape factor on convective heat transfer and energetic performance of water-based SiO_2 and ZnO nanofluids. Appl Therm Eng 51:839–851
26. Ellahi R, Hassan M, Zeeshan A, Khan AA (2016) The shape effects of nanoparticles suspended in HFE-7100 over wedge with entropy generation and mixed convection. Appl Nanosci 6(5):641–651
27. Karimi-Nazarabad M, Goharshadi EK, Youssefi A (2016) Particle shape effects on some of the transport properties of tungsten oxide nanofluids. J Mol Liq 223:828–835
28. Sheikholeslami M, Bhatti MM (2017) Forced convection of nanofluid in presence of constant magnetic field considering shape effects of nanoparticles. Int J Heat Mass Transf 111:1039–1049
29. Monfared M, Shahsavar A, Bahrebar MR (2019) Second law analysis of turbulent convection flow of boehmite alumina nanofluid inside a double-pipe heat exchanger considering various shapes for nanoparticle. J Therm Anal Calorim 135(2):1521–1532
30. Al-Rashed AAAA, Ranjbarzadeh R, Aghakhani S, Soltanimehr M, Afrand M, Nguyen TK (2019) Entropy generation of boehmite alumina nanofluid flow through a minichannel heat exchanger considering nanoparticle shape effect. Phys A. https://doi.org/10.1016/j.physa.2019.01.106
31. Alsarraf J, Moradikazerouni A, Shahsavar A, Afrand M, Salehipour H, Tran MD (2019) Hydrothermal analysis of turbulent boehmite alumina nanofluid flow with different nanoparticle shapes in a minichannel heat exchanger using two-phase mixture model. Physica A 520:275–288
32. Sadripour S, Chamkha AJ (2019) The effect of nanoparticle morphology on heat transfer and entropy generation of supported nanofluids in a heat sink solar collector. Therm Sci Eng Prog 9:266–280
33. Shahsavar A, Rahimi Z, Salehipour H (2019) Nanoparticle shape effects on thermal-hydraulic performance of boehmite alumina nanofluid in a horizontal double-pipe minichannel heat exchanger. Heat Mass Transf 55(6):1741–1751
34. Kaloudis E, Papanicolaou E, Belessiotis V (2016) Numerical simulations of a parabolic trough solar collector with nanofluid using a two-phase model. Renew Energy 97:218–229
35. Benabderrahmane A, Benazza A, Laouedj S, Solano JP (2017) Numerical analysis of compound heat transfer enhancement by single and two-phase models in parabolic through solar receiver. Mechanika 23(1):55–61
36. Borgnakke C, Sonntag RE (2018) Fundamentals of thermodynamics, 7th edn. Wiley, New York
37. Sadripour S (2019) 3D numerical analysis of atmospheric-aerosol/carbon-black nanofluid flow within a solar air heater located in Shiraz, Iran. Int J Num Methods Heat Fluid Flow 29(4):1378–1402
38. Dudley V, Kolb G, Sloan M, Kearney D (1994) SEGS LS2 Solar Collector Test Results, Report of Sandia National Laboratories, Report No. 94-1884
39. Dow Chemical Company, Syltherm 800 Heat Transfer Fluid, Product Technical Data, Dow, 1997
40. Corcione M (2011) Empirical correlating equations for predicting the effective thermal conductivity and dynamic viscosity of nanofluids. Energy Convers Manag 52:789–793
41. Keblinski P, Phillpot SR, Choi SUS, Eastman JA (2002) Mechanisms of heat flow in suspensions of nano-sized particles (nanofluids). Int J Heat Mass Transf 45:855–863
42. Incropera FP, Dewitt DP, Bergman TL, Lavine AS (2006) Fundamentals of heat and mass transfer, 6th edn. Wiley, New York
43. Chandra YP, Singh A, Mohapatra SK, Kesari JP, Rana L (2017) Numerical optimization and convective thermal loss analysis of improved solar parabolic trough collector receiver system with one sided thermal insulation. Sol Energy 148:36–48
44. Padilla RV, Demirkaya G, Goswami DY, Stefanakos E, Rahman MM (2011) Heat transfer analysis of parabolic trough solar receiver. Appl Energy 88:5097–5110
45. Schlunder EU (1983) Heat exchanger design handbook, vol 4. Hemisphere Publication Corporation, Washington, DC
46. Gnielinsli V (2009) Heat transfer coefficients for turbulent flow in concentric annular ducts. Heat Transf Eng 30(6):431–436
47. Siegel R, Howell JR (1971) Thermal radiation heat transfer. McGraw-Hill, New York
48. Dushman S (1962) Scientific foundations of vacuum technique. Wiley, New York
49. Kakat S, Shah RK, Aung W (1987) Handbook of single-phase convective heat transfer. Wiley, New York
50. ANSYS Inc (2009) Ansys CFX-solver theory guide. ANSYS Inc, Canonsburg
51. Behzadmehr A, Saffar-Avval M, Galanis N (2007) Prediction of turbulent forced convection of a nanofluid in a tube with uniform heat flux using a two phase approach. Int J Heat Fluid Flow 28:211–219
52. Hejazian M, Moraveji MK, Beheshti A (2014) Comparative study of Euler and mixture models for turbulent flow of Al_2O_3 nanofluid inside a horizontal tub. Int Commun Heat Mass Transf 52:152–158
53. Goktepe S, Atalk K, Ertrk H (2014) Comparison of single and two-phase models for nanofluid convection at the entrance of a uniformly heated tube. Int J Therm Sci 80:83–92
54. Patankar SV (1980) Numerical heat transfer and fluid flow. Taylor & Francis Group, Milton Park
55. Schiller L, Naumann A (1935) A drag coefficient correlation. Z Ver Dtsch Ing 77:318–320

56. He YL, Xiao J, Cheng ZD, Tao YB (2011) A MCRT and FVM coupled simulation method for energy conversion process in parabolic trough solar collector. Renew Energy 36:976–985
57. Sadaghiyani OK, Pesteei SM, Mirzaee I (2013) Numerical study on heat transfer enhancement and friction factor of LS-2 parabolic solar collector. J Therm Sci Eng Appl 6:012001–012010
58. Cheng Z, He Y, Xiao J, Tao Y, Xu R (2010) Three-dimensional numerical study of heat transfer characteristics in the receiver tube of parabolic trough solar collector. Int Commun Heat Mass Transf 37:782–787
59. Cheng Z, He Y, Cui F, Xu R, Tao Y (2012) Numerical simulation of a parabolic trough solar collector with non-uniform solar flux conditions by coupling FVM and MCRT method. Sol Energy 86:1770–1784
60. Sokhansefat T, Kasaeian A, Kowsary F (2014) Heat transfer enhancement in parabolic trough collector tube using Al_2O_3/synthetic oil nanofluid. Renew Sustain Energy Rev 33:636–644
61. Khakrah HR, Shamloo A, Kazemzadeh Hannani S (2018) Exergy analysis of parabolic trough solar collectors using Al_2O_3/synthetic oil nanofluid. Sol Energy 173:1236–1247
62. Sadripour S, Abbasian Arani AA, Kermani S (2018) Energy and exergy analysis and optimization of a heat sink collector equipped with rotational obstacles. AUT J Mech Eng 2(1):39–50